

Constructing Synchronously Rotating Double White Dwarf Binaries

Wesley Even and Joel E. Tohline

Department of Physics and Astronomy, Louisiana State University, Baton Rouge, LA 70803

ABSTRACT

We have developed a self-consistent-field technique similar to the one described by Hachisu, Eriguchi, & Nomoto (1986b) that can be used to construct detailed force-balanced models of synchronously rotating, double white dwarf (DWD) binaries that have a wide range of total masses, mass ratios, and separations. In addition to providing a computational tool that can be used to provide quiet initial starts for dynamical studies of the onset of mass transfer in DWD systems, we show that this SCF technique can be used to construct model sequences that mimic the last portion of the detached inspiral phase of DWD binary evolutions, and semi-detached model sequences that mimic a phase of conservative mass transfer.

Subject headings: binaries: close (AM CVn), hydrodynamics, methods: numerical, white dwarfs, supernovae

1. Introduction

As Webbink (1984) and Iben & Tutukov (1984, 1986) have pointed out, double white dwarf (DWD) binaries are expected to be the end product of the thermonuclear evolution of a sizeable fraction of all binary systems. The subset of DWD binaries that are born with orbital periods $P_{\text{orb}} \lesssim 5$ hours are of particular astrophysical interest because they will be driven into contact within a Hubble time via the loss of angular momentum through gravitational radiation (Paczynski 1967). Even this short-period component of the DWD population is expected to be quite large in our Galaxy. Sufficiently large that, according to Hills et al. (1990) and Cornish & Larson (2003), DWDs are likely to be a dominant source of background noise for the proposed *Laser Interferometer Space Antenna (LISA)* (Faller & Bender 1984; Evans et al. 1987; Bender 1998) in its lower gravitational-wave frequency band, $f_{\text{GW}} = 2/P_{\text{orb}} \lesssim 3 \times 10^{-3}$ Hz. Ironically, it is difficult to detect DWDs via traditional observational techniques because the intrinsic photon luminosity of white dwarfs is very low.

Broadly speaking, our Galaxy's DWD binary population should be dominated by systems that are in two distinctly different evolutionary phases: the inspiral phase alluded to above, during which both stars are detached from their respective Roche lobes; and a semi-detached, stable mass transfer phase, during which the less massive star fills its Roche lobe and is slowly transferring mass to its more massive companion. To date ~ 100 detached systems have been identified (Napiwotzki et al.

2001, 2004). Orbital periods and component masses have been determined for approximately one quarter of this sample (Marsh 2000; Maxted et al. 2000; Napiwotzki et al. 2002; Karl et al. 2003; Nelemans et al. 2005). AM CVn is the prototype of semi-detached DWD systems that are undergoing a phase of stable mass transfer (Warner 1995). In the immediate solar neighborhood ~ 20 such systems are known (Woudt & Warner 2003; Nelemans 2005; Anderson et al. 2005; Roelofs et al. 2005; Ramsay et al. 2007).

Theoretical arguments suggest that the ultimate fate of a DWD binary will depend on the system’s total mass, M_{tot} , and mass ratio q_0 at the onset of mass transfer (Marsh et al. 2004; Gokhale, Peng & Frank 2007; Frank 2008). For example, a DWD will likely only be able to enter an extended phase of stable mass transfer as characterized by AM CVn systems if q_0 is less than some critical value q_{stable} — where q_{stable} is almost certainly $\leq 2/3$ and may be closer to $1/4$. If $q_0 > q_{\text{stable}}$, the mass transfer rate is expected to diverge in a finite time, ultimately implying tidal disruption of the donor and/or a catastrophic merger of the two components. Consistent with the theoretical ideas presented by Webbink (1984) and Iben, Tutukov & Yungelson (1996), recent observations strongly suggest that the end product of some DWD mergers are R Coronae Borealis (RCB) stars and hydrogen-deficient carbon (HdC) stars (Clayton et al. 2007). Also, DWD systems with M_{tot} in excess the Chandrasekhar mass have long been considered likely progenitors of Type Ia supernovae (Webbink 1984; Iben, Tutukov & Yungelson 1996; Livio 2000; Yoon et al. 2007).

Over the past couple of decades, various groups have employed smoothed particle hydrodynamics (SPH) techniques to illustrate the dynamical behavior of DWD systems that violently merge after encountering an unstable mass-transfer event (Benz et al. 1990; Rasio & Shapiro 1995; Segretain, Chabrier, & Mochkovitch 1997; Fryer et al. 1999; Guerrero, Garcia-Berro, & Isern 2004; Yoon et al. 2007). Typically, initial states for these simulations have been constructed in such a way that the merger process is completed in $\lesssim 5$ orbits after first contact. D’Souza et al. (2006) and Motl et al. (2007) recently employed a grid-based finite-volume (FV) computational fluid dynamic technique to also study the onset and nonlinear development of mass transfer in strongly interacting binary systems. Their primary objective was to ascertain the value of q_{stable} in systems, such as DWDs, that undergo a phase of direct impact accretion following the onset of mass transfer. They were able to follow the evolution of a couple of different systems through $\gtrsim 30$ orbits. Instead of merging, these systems appeared to be entering a long-term phase of stable mass transfer. Presumably these are the types of binary configurations that serve as the progenitors of AM CVn systems.

Motl et al. (2007) found that the outcome of their simulations — for example, whether a system survives the onset of mass transfer or merges — can be sensitive to initial conditions. In particular if, rather than making only marginal contact with its Roche lobe, the donor star is in relatively deep contact at the onset of a simulation, the mass-transfer rate will initially be artificially high and it may be difficult for the system to avoid merger. As a result, a DWD system that should be categorized by numerical simulation as an AM CVn progenitor may be incorrectly categorized as a likely progenitor of an RCB star or a Type Ia supernova. It is therefore important to start such

simulations from initial states that are very quiet — that is, from initial configurations that are in detailed force balance throughout — and to perform each simulation with a grid (or particle) resolution that is sufficient to resolve marginal, or at least very shallow, contact between the donor and its Roche lobe. In two very recent reports, Fryer & Diehl (2008) and Dan, Rosswog, & Brüggen (2008) have confirmed this finding. Both groups have shown that SPH techniques also can be used to follow stable mass-transfer events through $\gtrsim 30$ orbits if sufficiently quiet initial states are used and if the simulations are carried out using a sufficiently large number of SPH particles.

Quiet initial states were constructed for the hydrodynamic simulations reported by D’Souza et al. (2006) and Motl et al. (2007) using a self-consistent-field (SCF) technique very similar to the one described by Hachisu (1986b). However, these initial models were constructed using a polytropic equation of state. Here we use a modified version of the SCF technique developed by Hachisu, Eriguchi, & Nomoto (1986b) for the zero temperature white dwarf (ZTWD) equation of state derived by Chandrasekhar (1935). We show how this SCF technique can be used to construct synchronously rotating, unequal-mass DWD binaries in which the less-massive (donor) star is in marginal contact with its Roche lobe and thereby provide excellent initial models for dynamical studies of interacting DWD systems that have a realistic equation of state.

To demonstrate the broad utility of this SCF technique, we construct a sequence of detached, synchronously rotating binaries of varying separation, but fixed mass ratio and constant total mass, to mimic the last portion of the inspiral phase of evolution of DWD binary systems. This enables us to determine, for example, the degree to which the functional dependence of the orbital frequency on orbital separation $\Omega(a)$ deviates from a pure Keplerian behavior. This type of sequence can be used to accurately identify the critical separation a_{crit} and corresponding orbital frequency at which the less massive component of a DWD binary first makes contact with its Roche lobe. Information of this nature will be helpful in interpreting future observations that are expected to be made with *LISA*, as described for example by Kopparapu & Tohline (2007). Finally, we show how this SCF technique can be used to construct a sequence of semi-detached binaries of fixed total mass, but varying separation and decreasing mass ratio, to mimic the initial stage of evolution of a DWD binary that has entered an AM CVn (*i.e.*, stable mass-transfer) phase of evolution.

2. SCF Formulation

The SCF technique was first introduced to the astrophysics community by Ostriker & Mark (1964) to create models of rapidly rotating, single stars with a polytropic equation of state. Hachisu developed a variation of the technique, improving convergence rates and extending its capabilities to include the use of a ZTWD equation of state. With his improved technique, Hachisu was able to construct two-dimensional (2D) configurations of differentially rotating, single white dwarfs (Hachisu 1986a) and three-dimensional (3D) configurations of uniformly rotating multiple white dwarf systems in which the stars have equal mass (Hachisu 1986b). New & Tohline (1997) employed Hachisu’s 3D technique to construct inspiral sequences of equal-mass DWD binaries, includ-

ing over-contact models having separations even smaller than a_{crit} . Hachisu (1986b) also applied his technique to the construction of unequal-mass binary systems using a polytropic equation of state and after additional algorithmic innovations were introduced, Hachisu, Eriguchi, and Nomoto (1986a,b) constructed a small sample of unequal-mass DWD binaries and heavy-disk white dwarf systems to examine the likely outcome of DWD mergers. In what follows we show how Hachisu’s SCF technique for constructing unequal-mass DWD binaries can be further improved and used to construct inspiral binary sequences.

2.1. Equation of State

In the zero-temperature white dwarf (ZTWD) equation of state (Chandrasekhar 1935, 1967; Hachisu 1986a) the electron degeneracy pressure P varies with the mass density ρ according to the relation,

$$P = A \left[x(2x^2 - 3)(x^2 + 1)^{1/2} + 3 \sinh^{-1} x \right], \quad (1)$$

where the dimensionless parameter,

$$x \equiv \left(\frac{\rho}{B} \right)^{1/3}, \quad (2)$$

and the constants A and B are (see Appendix A and Table A1 for elaboration),

$$A \equiv \frac{\pi m_e^4 c^5}{3h^3} = 6.00228 \times 10^{22} \text{ dynes cm}^{-2}, \quad (3)$$

$$\frac{B}{\mu_e} \equiv \frac{8\pi m_p}{3} \left(\frac{m_e c}{h} \right)^3 = 9.81011 \times 10^5 \text{ g cm}^{-3}. \quad (4)$$

According to Chandrasekhar (1967) (see again our Appendix A), a natural length scale associated with models of ZTWDs is,

$$\mu_e \ell_1 = \left(\frac{2A}{\pi G} \right)^{1/2} \frac{\mu_e}{B} = 7.71395 \times 10^8 \text{ cm} = 0.0111 R_\odot, \quad (5)$$

and the associated limiting white dwarf mass is,

$$\mu_e^2 M_{\text{ch}} = 4\pi(2.01824) \left(\frac{2A}{\pi G} \right)^{3/2} \left(\frac{\mu_e}{B} \right)^2 = 1.14205 \times 10^{34} \text{ g} = 5.742 M_\odot. \quad (6)$$

Throughout this work, we will assume that the average ratio of nucleons to electrons throughout each white dwarf is $\mu_e = 2$. Hence, $B = 1.96202 \times 10^6 \text{ g cm}^{-3}$, $\ell_1 = 5.55 \times 10^{-3} R_\odot$, and $M_{\text{ch}} = 1.435 M_\odot$.

In terms of the enthalpy of the gas,¹

$$H \equiv \int \frac{dP}{\rho}, \quad (7)$$

the ZTWD equation of state shown in Eq. (1) can also be written in the form,

$$H = \frac{8A}{B} \left[x^2 + 1 \right]^{1/2}. \quad (8)$$

Inverting this gives the dependence of ρ on H , namely,

$$\frac{\rho}{B} = x^3 = \left[\left(\frac{BH}{8A} \right)^2 - 1 \right]^{3/2}. \quad (9)$$

As a foundation for both constructing and understanding the structures of the synchronously rotating and tidally distorted stars in ZTWD binary systems, we have regenerated Chandraskehar’s spherical white dwarf sequence using a variation of the SCF technique outlined by Hachisu (1986a). As is discussed in §3.1, Table 2 details key properties of the ZTWD structures that lie along this spherical model sequence. The white dwarf mass-radius relationship that is derived from models along this sequence is illustrated by the diamonds in Figure 1. For comparison, results from the published spherical sequence of Hachisu (1986a) are represented in this figure by asterisks and the solid curve shows the approximate, analytic mass-radius relationship, Eq. (A14), derived for ZTWD stars by Nauenberg (1972). (As explained in Appendix A, it is more appropriate for us to compare our results to this “Nauenberg” mass-radius relation than to the more widely used “Eggleton” mass-radius relation, shown in Eq. A16.)

2.2. Binary System Geometry and Governing Equations

Our objective is to determine the 3D structure of a pair of ZTWD stars that are in a tight, circular orbit under the condition that both stars are synchronously rotating with the binary orbital frequency Ω . We begin by specifying the masses M_1 and M_2 of the primary and secondary stars, respectively, such that $M_2 \leq M_1$. Alternatively, we can specify the total system mass $M_{\text{tot}} \equiv M_1 + M_2$ and the system mass ratio $q \equiv M_2/M_1 \leq 1$, in which case,

$$\begin{aligned} M_1 &= \left(\frac{1}{1+q} \right) M_{\text{tot}}, \\ M_2 &= \left(\frac{q}{1+q} \right) M_{\text{tot}}. \end{aligned}$$

Figure 2 shows a slice through the equatorial plane of such a system under the assumption that both stars are spherically symmetric. For our final equilibrium models in which the effects of

¹As defined here, H is actually enthalpy per unit mass.

tidal and rotational distortions are taken into account in a fully self-consistent fashion, this figure provides only a schematic illustration of the binary system’s equatorial-plane structure. However, it provides an accurate depiction of the equatorial-plane structure of the initial stellar models that are fed into our iterative SCF scheme (see §2.3).

In Figure 2, the more massive, primary star is shown on the left and the less massive, secondary star is on the right; the centers of the stars are located a distance ϖ_1 and ϖ_2 , respectively, from the center of mass of the binary system; and the binary separation $a = \varpi_1 + \varpi_2$. Because we are using a ZTWD equation of state, the central density ρ_{\max}^i and radius R_i of each star ($i = 1, 2$) cannot be specified independently of each star’s chosen mass. As an initial guess for our SCF technique, the values of $\rho_{\max}^{i=1}$, $\rho_{\max}^{i=2}$, R_1 , and R_2 are drawn from Table 2, that is, they are given by values that correspond to spherical ZTWDs having masses M_1 and M_2 .

For various values of the three principal system parameters M_1 , M_2 and a , our specific aim is to determine in a self-consistent fashion on a cylindrical coordinate mesh (ϖ, θ, Z) , the values and spatial distribution of the scalar fields $\rho^i(\varpi, \theta, Z)$, $H^i(\varpi, \theta, Z)$, and $P^i(\varpi, \theta, Z)$, for both stars ($i = 1, 2$) in synchronously rotating, ZTWD binaries. Following Hachisu (1986a,b) and Hachisu, Eriguchi, and Nomoto (1986a,b), in order to construct these desired binary configurations we need to solve the following five equations simultaneously:

$$\nabla^2 \Phi(\varpi, \theta, z) = 4\pi G \sum_i \rho^i(\varpi, \theta, z), \quad (10)$$

$$C^i = H^i(\varpi, \theta, z) + \Phi(\varpi, \theta, z) - \frac{1}{2}\Omega^2 \varpi^2, \quad (11)$$

$$\rho^i(\varpi, \theta, z) = B[x^i(\varpi, \theta, z)]^3 = B \left\{ \left[\frac{B}{8A} H^i(\varpi, \theta, z) \right]^2 - 1 \right\}^{3/2}, \quad (12)$$

where $\Phi(\varpi, \theta, Z)$ is the Newtonian gravitational potential of the combined stellar system, and $C^{i=1}$ and $C^{i=2}$ are constants that specify the conditions of the Bernoulli flow inside each star.

2.3. Solution Strategy

Our solution strategy follows closely the methods described in Hachisu (1986b) and Hachisu, Eriguchi, & Nomoto (1986b) so only the differences between our methods will be given in detail here. The variables with a carat ($\hat{\cdot}$) above them are the dimensionless version of the variables as defined in Eqs.(22)-(27) of Hachisu (1986b).

To begin an SCF iteration two spherical stars are initially placed on the computational grid in such a way that the center of mass of the system falls at the origin of the coordinate system and the outer edge of the secondary star (point O_α in Figure 2) is at $\hat{\varpi} = 1$. The centers of the stars are therefore located, respectively, at

$$\hat{\varpi}_1 \equiv \frac{\varpi_1}{\varpi_\alpha} = \frac{q}{1 + \ell(1 + q)}, \quad (13)$$

$$\hat{\varpi}_2 \equiv \frac{\varpi_2}{\varpi_\alpha} = \frac{1}{1 + \ell(1 + q)}, \quad (14)$$

where the dimensionless ratio $\ell \equiv R_2/a$ is known once M_2 and a have been chosen. These two expressions make sense because $\varpi_\alpha = (\varpi_2 + a\ell) = [\varpi_2 + (\varpi_2 + \varpi_1)\ell]$ and, for a point-mass binary whose center of mass is at the origin of the grid, $\varpi_1 = q\varpi_2$. With $\hat{\rho}^i$ defined everywhere on the grid, $\hat{\Phi}(\hat{\varpi}, \theta, \hat{z})$ is calculated via Eq. (10). In this work the boundary values for $\hat{\Phi}$ are calculated using the compact cylindrical Green’s function expansion described in Cohl & Tohline (1999), and the values of the potential throughout the interior volume of the computational grid are calculated using the Krylov subspace methods provided by the PETSc software library (Balay et al. 2004).

During each iteration, the interior structure of the secondary star is calculated using the same strategy as outlined in §2b of Hachisu, Eriguchi, & Nomoto (1986b). To update the structure of the primary star, however, the location of $\hat{H}_{max}^{i=1}$ is used instead of specifying the inner edge of the star, as was done in Hachisu, Eriguchi, & Nomoto (1986b). This choice eliminates the extra iterative steps that were needed when the third boundary condition was specified at the inner edge of the primary star. Using Eq. (8), we determine the value of the normalized enthalpy at the center of the primary star from the values of x_{max}^i selected for both stars and the value of $\hat{H}_{max}^{i=2}$ just derived for the secondary star. Specifically, we set

$$\hat{H}_{max}^{i=1} = \hat{H}_{max}^{i=2} \left[\frac{(x_{max}^{i=1})^2 + 1}{(x_{max}^{i=2})^2 + 1} \right]^{1/2}. \quad (15)$$

Then we determine the value of the Bernoulli constant inside the primary star by examining the distribution of the variable \hat{F} as defined in Eq.(48) of Hachisu (1986a), that is,

$$\hat{F}^i \equiv -\hat{\Phi} + \frac{1}{2}\hat{\Omega}^2\hat{\varpi}^2 = (\hat{H}^i - \hat{C}^i). \quad (16)$$

In the vicinity of the original center of the primary star, that is, in the vicinity of point O_1 as illustrated in Figure 2, the function \hat{F} should exhibit a local maximum. We associate the location of this local maximum with the updated position of point O_1 and we set $\hat{F}_{max}^{i=1}$ equal to the value of the function at this local maximum. We therefore deduce from Eq. (16) that,

$$\hat{C}^{i=1} = \hat{H}_{max}^{i=1} - \hat{F}_{max}^{i=1}. \quad (17)$$

With this constant in hand, the normalized enthalpy throughout the primary star can be determined via the expression,

$$\hat{H}^{i=1} = \hat{C}^{i=1} + \hat{F}^{i=1}, \quad (18)$$

and we obtain an updated “guess” for the normalized density distribution inside the primary star via the expression,

$$\hat{\rho}^{i=1} = \frac{1}{(x_{max}^{i=2})^3} \left\{ \left(\frac{\hat{H}^{i=1}}{\hat{H}_{max}^{i=1}} \right)^2 [(x_{max}^{i=1})^2 + 1] - 1 \right\}^{3/2}. \quad (19)$$

2.4. Global Properties and Convergence

Our iterative scheme is judged to be operating well if various calculated model parameters — such as the dimensionless stellar masses \hat{M}^i and Bernoulli constants \hat{C}^i — converge toward well-defined values. We also have found it useful to track the convergence of various global energy parameters. Specifically, at the end of each iteration cycle we calculate the dimensionless rotational kinetic energy \hat{K} , gravitational potential energy \hat{W} , total internal energy \hat{U} (see, for example, Eq. (75') in Chapter *XI* of Chandrasekhar (1967)), and globally averaged pressure $\hat{\Pi}$ of the model, defined as follows:

$$\hat{K} \equiv \int \frac{1}{2} \hat{\Omega}^2 \hat{\omega}^2 \hat{\rho} d\hat{V}, \quad (20)$$

$$\hat{W} \equiv \int \frac{1}{2} \hat{\phi} \hat{\rho} d\hat{V}, \quad (21)$$

$$\hat{U} \equiv \int \left[\left(\hat{H} - \frac{8A}{B} \right) \hat{\rho} - \hat{P} \right] d\hat{V}, \quad (22)$$

$$\hat{\Pi} \equiv \int \hat{P} d\hat{V}. \quad (23)$$

where $d\hat{V} = \hat{\omega} d\hat{\omega} d\theta d\hat{z}$ is the dimensionless differential volume element on our cylindrical grid. Then the system's dimensionless total energy is given by the sum,

$$\hat{E}_{\text{tot}} \equiv \frac{E_{\text{tot}}}{G(\rho_{\text{max}}^{i=2})^2 \varpi_*^5} = \hat{K} + \hat{W} + \hat{U}, \quad (24)$$

and, if the model has converged to a proper equilibrium state, according to the virial theorem we should expect,

$$2\hat{K} + \hat{W} + 3\hat{\Pi} = 0. \quad (25)$$

In general, at each iteration step the condition of virial equilibrium, Eq. (25), will not be satisfied, but if our iteration scheme is well behaved, convergence toward the virial condition should be achieved. With this in mind, we have found that the virial error,

$$VE \equiv \left| \frac{2\hat{K} + \hat{W} + 3\hat{\Pi}}{\hat{W}} \right|, \quad (26)$$

provides a meaningful measure of the quality of each model.

We declare that satisfactory convergence to a given model has been achieved when the absolute value of the fractional change between iterations has dropped below a specified convergence criterion, $\delta \sim 10^{-4}$, for all of the following quantities: \hat{C}^i , \hat{M}^i , $\hat{\Omega}$, \hat{K} , \hat{W} , $\hat{\Pi}$, and the physical value of ϖ_α . In addition, the converged model is judged to be a good equilibrium state if the virial error, VE, is sufficiently small. Table 1 illustrates how we were able to achieve a lower virial error and, hence, a more accurate representation of an equilibrium configuration, by improving the grid resolution and/or by specifying a tighter convergence criterion. Specifically, the table shows that as

we were constructing binary model B3 (see discussion associated with Table 6, below) we were able to push the VE down from a value $\sim 5 \times 10^{-3}$ to a value $\sim 5 \times 10^{-4}$ by increasing the grid resolution from (64,128,33) to (128,256,65) zones in $(\hat{\varpi}, \theta, \hat{z})$ and by pushing δ from 10^{-2} to 3.5×10^{-5} .

After the SCF code has converged to the desired equilibrium model, the various dimensionless variables are converted back to proper physical units following, for example, the scalings presented in Eqs.(22)-(27) of Hachisu (1986a). We note in particular that the value of the scale length $\varpi_* = \varpi_\alpha$ is obtained by evaluating a dimensionless version of Eq. (8) for the secondary star in combination with Eq.(27) from Hachisu (1986a), which gives,

$$\varpi_* = \left[\frac{8A/B}{G\rho_{max}^{i=2}} \right]^{1/2} (\hat{H}_{max}^{i=2})^{-1/2} \left[(x_{max}^{i=2})^2 + 1 \right]^{1/4}. \quad (27)$$

In addition to the physical variables already identified, for each converged model we have found it useful to evaluate the system’s total angular momentum,

$$J_{\text{tot}} \equiv \int \varpi^2 \Omega \rho dV, \quad (28)$$

as well as the spin angular momentum of each component star, J_{spin}^i , and each star’s Roche-lobe filling factor, f_{RL}^i . As with the determination of quantities such as M^i and R^i , these latter two quantities are obtained by performing volume integrals over appropriate sub-domains of the computational grid, determined as follows. Let the origin of a Cartesian grid coincide with the center of mass of the binary system and align the x -axis of that grid with the line that connects the centers of the two stars as illustrated in Figure 2. Between points O_1 and O_2 along this axis, the effective potential,

$$\Phi_{\text{eff}}(x) \equiv \Phi(x) - \frac{1}{2} \Omega^2 x^2, \quad (29)$$

will exhibit a maximum at position x_{L1} associated with the inner “L1” Lagrange point. We define sub-domain $\mathcal{D}_*^{i=2}$ as the volume of the grid for which $x \equiv \varpi \cos \theta \geq x_{L1}$ and $\rho > 0$, that is, the region occupied by the secondary star; and we define sub-domain $\mathcal{D}_*^{i=1}$ as the volume of the grid for which $x < x_{L1}$ and $\rho > 0$, that is, the region occupied by the primary star. Then the mass of each star is determined by the integral,

$$M^i = \int_{\mathcal{D}_*^i} \rho^i dV, \quad (30)$$

the volume occupied by each star is,

$$\mathcal{V}_*^i = \int_{\mathcal{D}_*^i} dV, \quad (31)$$

and the spin angular momentum of each star is given by the expression,

$$J_{\text{spin}}^i \equiv \int_{\mathcal{D}_*^i} [\varpi^2 \sin^2 \theta + (\varpi \cos \theta - \varpi_i)^2] \Omega \rho^i dV. \quad (32)$$

Having determined the volumes \mathcal{V}^i occupied by both rotationally flattened and tidally distorted stars, we define the mean radius of each star as,

$$R^i = \left(\frac{3\mathcal{V}_*^i}{4\pi} \right)^{1/3}. \quad (33)$$

We furthermore define sub-domain $\mathcal{D}_{\text{RL}}^{i=2}$ as the volume of the grid for which $x \geq x_{L1}$ and $\Phi_{\text{eff}} \leq \Phi_{\text{eff}}(x_{L1})$, and sub-domain $\mathcal{D}_{\text{RL}}^{i=1}$ as the volume of the grid for which $x < x_{L1}$ and $\Phi_{\text{eff}} \leq \Phi_{\text{eff}}(x_{L1})$. Then the Roche-lobe volume surrounding each star is,

$$\mathcal{V}_{\text{RL}}^i = \int_{\mathcal{D}_{\text{RL}}^i} dV, \quad (34)$$

and each star’s Roche-lobe filling factor is obtained from the ratio,

$$f_{\text{RL}}^i = \frac{\mathcal{V}_*^i}{\mathcal{V}_{\text{RL}}^i}. \quad (35)$$

3. Results

3.1. Single White Dwarfs

As mentioned earlier, we initially used a simplified version of our SCF code to construct a large number of single, nonrotating white dwarfs in order to compare our solutions with previous results (see Figure 1) and to provide initial guesses for the density distributions inside both stars in each binary system. Table 2 details the properties of single, nonrotating white dwarfs that have central densities ranging from $10^{4.5}$ g cm $^{-3}$ to 10^{10} g cm $^{-3}$ as determined from our model calculations; the 23 selected models are equally spaced in units of $\log \rho_{\text{max}}$. These spherical models were constructed on a uniform cylindrical mesh with resolution (128, 128, 128) in $(\hat{\varphi}, \theta, \hat{z})$ using a convergence criterion $\delta = 10^{-4}$. For each converged model, the first six columns of Table 2 list, respectively, the star’s mass M in solar masses, radius R in units of 10^8 cm, central density ρ_{max} in g cm $^{-3}$, corresponding value of $x_{\text{max}} = (\rho_{\text{max}}/B)^{1/3}$, moment of inertia,

$$I = \int \varpi^2 \rho dV, \quad (36)$$

in units of 10^{50} g cm 2 , and the radius of gyration, $k \equiv I/(MR^2)$. As shown in the last column of Table 2, a typical virial error for these converged models was $10^{-4} - 10^{-5}$. The values tabulated for the radius of gyration vary smoothly from $k = 0.2036$ for $M = 0.0844M_{\odot}$ to $k = 0.1013$ for $M = 1.4081M_{\odot}$. This is consistent with our understanding that low-mass white dwarfs have structures similar to $n = 3/2$ polytropes for which $k = 0.205$ (Ruciński 1988), while high-mass white dwarfs display structures similar to $n = 3$ polytropes for which $k = 0.0758$ (Ruciński 1988). Our values of k over this range of stellar masses are also consistent with the analytic function for

$k(M)$ that Marsh et al. (2004) fit through similar spherical model data. Knowledge of the radius of gyration of these spherical ZTWD models has assisted us in analyzing the tidally distorted structures that arise in our models of synchronously rotating white dwarfs in close binary systems (see further discussion, below).

Using this same three-dimensional, cylindrical coordinate grid we constructed nonrotating models with central densities above $10^{10} \text{ g cm}^{-3}$, that is, with masses above $1.4M_{\odot}$. We have not included these higher mass models in Table 2 or Figure 1, however, because they did not converge to satisfactorily accurate structures. In particular, as the mass was steadily increased above $1.4M_{\odot}$, the models converged to structures with steadily increasing (rather than decreasing) values of k . By contrast, models constructed using a one-dimensional spherical code with much higher spatial resolution displayed values of k that decreased steadily to a value of 0.0755 at masses approaching M_{ch} . If desired, the three-dimensional computational grid resolution could be increased to produce more accurate models of the white dwarf structure near the Chandrasekhar mass limit.

3.2. White Dwarf Binary Sequences

The slow inspiral evolution of a DWD binary can be mimicked by constructing a sequence of detached binaries having fixed M_{tot} and fixed q but varying separation, down to the separation at which the less massive star first makes contact with its Roche lobe. In an effort to illustrate the capabilities of our code, we have constructed three binary sequences having the same total mass — namely, $M_{\text{tot}} = 1.5M_{\odot}$ — but three separate mass ratios. Specifically, sequence ‘A’ has $q = 1$, sequence ‘B’ has $q = 2/3$, and sequence ‘C’ has $q = 1/2$. As detailed in Table 3, spherical models were constructed with the desired primary and secondary masses for these three sequences — specifically, $M = 0.5M_{\odot}, 0.6M_{\odot}, 0.75M_{\odot}, 0.9M_{\odot}$ and $1.0M_{\odot}$ — to provide good “guesses” for the initial binary star density distributions to start each SCF iteration. In addition to listing the values of M , R , ρ_{max} , x_{max} , and k for each of these converged spherical models, as was done for a wider range of spherical models in Table 2, Table 3 also lists values for the global energies W , U , and Π in units of 10^{50} ergs.

Along each sequence, all the binary models were constructed using a uniform cylindrical grid with (128,256,65) zones in $(\hat{\varphi}, \theta, \hat{z})$; by implementing reflection symmetry through the equatorial plane, only half as many zones were needed in the vertical direction as in the radial direction to achieve the same resolution in both. No additional symmetries were assumed in constructing the sequence, although, for the models shown here, symmetry through the x-z plane also could have been implemented for additional savings. The convergence criterion was set to $\delta = 2.5 \times 10^{-4}$; in most models, $\hat{\Omega}$ was the last variable to converge to this desired level. We note that, because the same number of grid zones was used for each model and each binary was scaled to fit entirely within the grid, the effective resolution of each star decreased as the binary separation a increased along each sequence.

Two tables have been produced for each DWD inspiral sequence in order to detail the properties of the models that lie along each sequence. For sequence ‘A’ ($q = 1$), for example, Table 4 lists the values of six global binary system parameters (a , Ω , M_{tot} , q , J_{tot} , E_{tot}) and the virial error obtained for thirty-five models (numbered *A1* through *A35*) whose binary separations vary from 2.0956×10^9 cm at contact (model *A1*) to 3.0911×10^9 cm (model *A35*). For this same group of models, Table 5 lists calculated values of five parameters (M_i , R_i , ρ_{max}^i , f_{RL}^i , J_{spin}^i) for the individual stellar components ($i = 1, 2$). Tables 6 and 7 provide the same detailed information for models along sequence ‘B’ ($q = 2/3$), and Tables 8 and 9 provide this information for models along sequence ‘C’ ($q = 1/2$).

The equatorial-plane density distributions displayed in Figures 3, 4, and 5 illustrate the degree to which both white dwarf components are distorted by tides for various binary separations along each sequence. Labels in the upper-right-hand corner of each figure panel identify each binary system according to its corresponding position along each sequence, as itemized in Tables 4 - 9. Along sequence ‘A’ (Figure 3), both components of the binary system are of equal size and display identical degrees of tidal distortion because the mass ratio $q = 1$. Along sequences ‘B’ and ‘C’ (Figures 4 and 5, respectively), however, the primary star (on the left in each figure panel) is noticeably smaller and less distorted than the secondary star.

Figure 6 has been constructed from the data detailed in Tables 4 and 5 for binary sequence ‘A.’ Specifically, the diamond symbols in the top two panels and in the bottom panel of this figure show, respectively, how the binary system’s total angular momentum, J_{tot} , total energy, E_{tot} , and orbital angular velocity, Ω , vary with orbital separation along this sequence; and the third panel from the top shows how the Roche-lobe filling factor, f_{RL}^i , varies with orbital separation for both the primary star (diamonds) and the secondary star (asterisks). Figures 7 and 8 have been similarly constructed from the data detailed, respectively, in Tables 6 and 7, and in Tables 8 and 9.

Following the lead of New & Tohline (1997), in constructing Figures 6 - 8 we have normalized our tabulated values of J_{tot} and E_{tot} to the quantities,

$$J_{\text{norm}} \equiv (GM_{0.75}^3 R_{0.75})^{1/2} = 4.0735 \times 10^{50} \text{ g cm}^2 \text{ s}^{-1}, \quad (37)$$

$$E_{\text{norm}} \equiv \frac{GM_{0.75}^2}{R_{0.75}} = 2.0119 \times 10^{50} \text{ erg}, \quad (38)$$

where $R_{0.75} = 7.4244 \times 10^8$ cm is the radius of a spherical ZTWD whose mass is $M_{0.75} = 0.7522 M_{\odot}$ as tabulated in Table 3. Also, at each separation our tabulated values of Ω have been normalized to the Keplerian orbital frequency,

$$\Omega_{\text{K}} = \left(\frac{2GM_{0.75}}{a^3} \right)^{1/2}. \quad (39)$$

In all three figures, values of the orbital separation have been specified (bottom horizontal axis) in units of 10^9 cm and (top horizontal axis) as normalized to the radius of a spherical ZTWD having the mass of the system’s secondary star as tabulated in Table 3, that is, $R_{0.75} \equiv 7.424 \times 10^8$ cm, $R_{0.60} = 8.671 \times 10^8$ cm and $R_{0.50} = 9.638 \times 10^8$ cm.

New & Tohline (1997) have previously constructed inspiral sequences for *equal-mass* DWD binary systems in which the structure of the individual component stars is governed by the Chandrasekhar ZTWD equation of state (1). The sequences published by New & Tohline (1997) cover a wide range of total masses. The one that most closely resembles our sequence ‘A’ (our only equal-mass sequence) has $M_{\text{tot}} = 1.63M_{\odot}$; the functional behavior of $E_{\text{tot}}(a)$ and $J_{\text{tot}}(a)$ for this sequence is presented in Figure 16 of New & Tohline (1997). Along this $M_{\text{tot}} = 1.63M_{\odot}$ sequence, the two stars first make contact with their respective Roche lobes at a normalized separation of approximately 2.825 (see also Figure 5 of New & Tohline 1997). This is completely consistent with the behavior of our sequence ‘A,’ where contact occurs (model A1) when $a/R_{0.75} = 2.823$.

The DWD sequences constructed by New & Tohline (1997) all extend to separations smaller than the point of first contact, as their SCF technique allowed them to build over-contact (common envelope) equal-mass binaries. Their functions $E_{\text{tot}}(a)$ and $J_{\text{tot}}(a)$ display a quadratic behavior along the over-contact segment of each sequence, passing through a minimum at a binary separation smaller than the point of first contact. None of our three sequences show this behavior because we have not attempted to construct models past the initial point of contact. Indeed, it seems unlikely that equilibrium configurations exist at smaller separations except when the system mass ratio is precisely $q = 1$.

For each of our DWD binary sequences, it is useful to compare the displayed functional behavior of $J_{\text{tot}}(a)$ from our numerical models against the behavior predicted by two simplified models. In the case of two point masses in circular orbit, the total angular momentum J_{pm} is given simply by the system’s orbital angular momentum, that is,

$$\begin{aligned} J_{\text{pm}} = J_{\text{orb}} &= M_1 \varpi_1^2 \Omega_K + M_2 \varpi_2^2 \Omega_K \\ &= \frac{q}{(1+q)^2} \left[GM_{\text{tot}}^3 a \right]^{1/2} \end{aligned} \quad (40)$$

This function, normalized to J_{norm} , is displayed by the solid curve in the top panels of Figures 6 - 8. An even more realistic representation of the function $J_{\text{tot}}(a)$ can be obtained by adding an approximate representation for the spin angular momentum, $I_i \Omega$, of both stars to the point-mass expression for J_{orb} . If we assume that both stars retain a spherical structure while spinning at the Keplerian orbital frequency, Ω_K , the appropriate expression for the total “spinning sphere” system angular momentum is,

$$\begin{aligned} J_{ss} &= J_{\text{orb}} + (I_1 + I_2) \Omega_K = J_{\text{orb}} + \left(k_1 M_1 R_1^2 + k_2 M_2 R_2^2 \right) \Omega_K \\ &= J_{\text{pm}} \left\{ 1 + \frac{(1+q)}{q} \left[k_1 \left(\frac{R_1}{a} \right)^2 + q k_2 \left(\frac{R_2}{a} \right)^2 \right] \right\}, \end{aligned} \quad (41)$$

where, in addition to q , values of (the constants) R_i and k_i appropriate for each binary sequence can be obtained from Table 3. Function (41), normalized to J_{norm} , is displayed by the dot-dashed curve in the top panels of Figures 6 - 8. Analytic expression (40) predicts that $J_{\text{tot}} \propto a^{1/2}$. Through

a correction factor, Eq. (41) displays a somewhat more complex behavior. Overall, our SCF model sequences match Eq. (41) particularly well. The largest deviation arises in all cases at the smallest separations; the slope of the SCF-generated $J_{\text{tot}}(a)$ function flattens somewhat as the secondary star approaches contact with its Roche lobe, that is, as $f_{\text{RL}}^{i=2} \rightarrow 1$.

The functional dependence of each system’s total energy, $E_{\text{tot}}(a)$, can be understood in a similar fashion. Considering only the kinetic and gravitational potential energy of two point masses in circular orbit, we obtain,

$$E_{\text{orb}} = K_{\text{orb}} + W_{\text{orb}} = -K_{\text{orb}} = -\frac{1}{2} \left[\frac{q}{(1+q)^2} \right] \frac{GM_{\text{tot}}^2}{a}, \quad (42)$$

where we have used the virial relation $(2K_{\text{orb}} + W_{\text{orb}}) = 0$. While this a^{-1} functional dependence explains the general $E_{\text{tot}}(a)$ behavior exhibited in Figures 6 - 8 by our numerically constructed model sequences, expression (42) is missing a nontrivial shift in the overall energy scale that is set by the binding energies of the two stars, namely,

$$E_{\text{b}} = \sum_{i=1}^2 \left(W^i + U^i \right). \quad (43)$$

Based on the properties of the spherical stellar models provided in Table 3, the appropriate energy shift for sequences ‘A,’ ‘B,’ and ‘C’ is, respectively, $E_{\text{b}} = -1.551 \times 10^{50}$ ergs, -1.698×10^{50} ergs, and -1.963×10^{50} ergs. Adding E_{b} to E_{orb} provides what we will refer to as the “point mass” total system energy,

$$E_{\text{pm}} = -\frac{1}{2} \left[\frac{q}{(1+q)^2} \right] \frac{GM_{\text{tot}}^2}{a} + E_{\text{b}}. \quad (44)$$

This analytic function, normalized to E_{norm} , is displayed as a solid curve in the plots of E_{tot} versus a shown in Figures 6 - 8. An improved approximation that we will refer to as the “spinning sphere” total system energy can be obtained by adding the rotational kinetic energy of both stars, assuming they remain spherically symmetric and spin uniformly with the Keplerian orbital frequency. Specifically,

$$\begin{aligned} E_{\text{ss}} &= E_{\text{pm}} + \sum_{i=1}^2 \left(\frac{1}{2} I_i \Omega_{\text{K}}^2 \right) \\ &= E_{\text{b}} + E_{\text{orb}} \left\{ 1 - \frac{(1+q)}{q} \left[k_1 \left(\frac{R_1}{a} \right)^2 + q k_2 \left(\frac{R_2}{a} \right)^2 \right] \right\}. \end{aligned} \quad (45)$$

This function, normalized to E_{norm} , is displayed as a dot-dashed curve in the plots of E_{tot} versus a shown in Figures 6 - 8. Expression (45) describes particularly well the variation of E_{tot} with separation displayed by our numerically constructed binary sequences ‘B’ and ‘C.’ We note, however, that all three of our sequences show that the total system energy drops slightly below the behavior predicted by Eq. (45) at the smallest separations.

The curve outlined by asterisks in the third panel from the top of Figures 6 - 8 shows that $f_{\text{RL}}^{i=2}$ steadily increases from a value ~ 0.2 to a value of 1.0 at the smallest separation along all three inspiral sequences, implying that the secondary star has made contact with its Roche lobe. For comparison, the curve outlined by diamonds in the same panel of these three figures shows how the Roche-lobe filling factor of the primary star varies along each sequence. The value of $f_{\text{RL}}^{i=1}$ does not climb above 0.063 for sequence ‘C’ or above 0.191 for sequence ‘B,’ reflecting the fact that in both cases the primary star is significantly more massive — and, hence, it has a significantly smaller radius — than the secondary star. For inspiral sequence ‘A,’ $f_{\text{RL}}^{i=1}(a)$ displays an identical behavior to $f_{\text{RL}}^{i=2}(a)$ because the primary and secondary stars have equal masses.

The bottom panel of Figures 6 - 8 displays the behavior of the normalized orbital frequency Ω/Ω_{K} as a function of binary separation derived from our three numerically constructed inspiral sequences. At the smallest separations, our models show that the orbital frequency is always $\sim 0.5\%$ higher than predicted by the “point-mass” Keplerian frequency. Our equal-mass sequence exhibits the largest deviation at contact; specifically, for model ‘A1,’ we find $\Omega = 1.0085 \Omega_{\text{K}}$. As the separation is increased along each sequence, the figures show that Ω/Ω_{K} approaches unity, as expected. However, at a sufficiently wide separation, each of our sequences displays a tiny discontinuous drop in the orbital frequency, followed by further decline that ultimately falls below the local Keplerian value. We suspect this odd behavior at wide separations arises from the discrete nature of our grid calculations coupled with progressively fewer grid zones falling inside both stars — resulting in progressively poorer numerical resolution — at wider separations.

3.3. Conservative Mass-Transfer Sequences

During a phase of stable mass transfer, a DWD binary system will evolve in such a way that the secondary star remains in marginal contact with its Roche lobe while it slowly transfers mass to the primary star. If the total mass of the system is conserved, then the evolution should proceed along a sequence of synchronously rotating configurations in which M_{tot} is constant, $f_{\text{RL}}^{i=2} = 1$, and q is steadily decreasing. Models *A1*, *B1* and *C1* can be viewed as representing three such configurations along a sequence whose total system mass is $M_{\text{tot}} = 1.5M_{\odot}$. In evolving from an initially equal-mass, contact configuration (model *A1*) to a semi-detached configuration with $q = 2/3$ (model *B1*), then on to a semi-detached configuration with $q = 1/2$ (model *C1*), the separation of such a system (measured in units of 10^9 cm) will increase from $a_9 = 2.10$, to $a_9 = 2.67$, then to $a_9 = 3.18$; and the system’s orbital period ($P_{\text{orb}} = 2\pi/\Omega$) will increase from 42.3 s to 61.0 s, then to 79.5 s.

It is clear, therefore, that our new SCF code can be used to construct model sequences that mimic the evolution of DWD systems undergoing slow, conservative mass-transfer. The models detailed in Tables 10 (sequence ‘D’) and 11 (sequence ‘E’) trace two such semi-detached sequences as the system mass ratio evolves from $q = 1$ to $q \lesssim 0.5$. For sequence ‘D,’ $M_{\text{tot}} = 1.5M_{\odot}$ and for sequence ‘E,’ $M_{\text{tot}} = 1.0M_{\odot}$. In the top two panels of Figures 9 and 10, data from Tables 10 and 11 have been plotted as diamond symbols to illustrate how a and Ω vary with q while $f_{\text{RL}}^{i=2}$ is held

to a value of unity (definition of a semi-detached binary) along these two fixed-mass sequences.

Up to now, the community has relied upon some relatively simple analytic expressions to approximate the behavior of, for example, $a(q)$ along conservative mass-transfer evolutionary trajectories. For example, by setting the radius of the secondary star as given by the Nauenberg mass-radius relation (A14) equal to the Roche-lobe radius R_{RL} as defined in terms of a and q by the approximate relation provided by Eggleton (1983), namely,

$$R_{\text{RL}} = a \left[\frac{0.49q^{2/3}}{0.6q^{2/3} + \ln(1 + q^{1/3})} \right], \quad (46)$$

one obtains,

$$\frac{a}{R_{\odot}} \approx 0.0229(n_2q^2)^{-1/3}(1 - n_2^{4/3})^{1/2} \left[0.6q^{2/3} + \ln(1 + q^{1/3}) \right], \quad (47)$$

where,

$$n_2 \equiv \frac{q}{(1 + q)} \left(\frac{M_{\text{tot}}}{M_{\text{ch}}} \right). \quad (48)$$

The function $a(q)$, defined by Eq. (47) for a given M_{tot} , has been plotted as a solid curve in the top panels of Figures 9 and 10, and the Keplerian orbital frequency associated with this separation (and relevant M_{tot}) has been plotted as a solid curve in the second panel of Figures 9 and 10. For both sequence ‘D’ and sequence ‘E,’ the analytically derived curves are consistently offset by 3 - 5% from our numerical model results. But overall, the analytically predicted functional behavior of $a(q)$ and $\Omega(q)$ is in very good agreement with our results. This is reassuring as it provides a degree of validation for both our numerical code and the approximations that were adopted by earlier investigators when deriving the more easily manipulated analytic expressions.

Finally, in the bottom two panels of Figures 9 and 10, the diamond symbols display the variation of J_{tot} and E_{tot} with q along sequence ‘D’ and sequence ‘E,’ respectively. The solid curve drawn in the $J_{\text{tot}}(q)$ panel of both figures shows the behavior predicted by our “spinning sphere” expression for the total system angular momentum (41) when used in conjunction with the $a(q, M_{\text{tot}})$ behavior prescribed by Eq. (47). Again, for a given M_{tot} there appears to be very good agreement between the functional behavior of $J_{\text{tot}}(q)$ displayed by our numerical model results and the analytic expressions. There is also a systematic offset between the two. In either case it is clear that, unlike the behavior displayed by $a(q)$ and $\Omega(q)$, the system’s total angular momentum does not vary monotonically with q along a conservative mass-transfer evolutionary trajectory. Note, in particular, that if the system mass ratio q is initially close to unity, J_{tot} *increases* as q decreases along the displayed trajectory. This result is unphysical. It signifies that slow evolution along a synchronously rotating, conservative mass-transfer trajectory can occur only if, at the onset of mass-transfer, $q < q_{\text{crit}}$, where the value of q_{crit} for a given M_{tot} is prescribed by the location of the maximum of the $J_{\text{tot}}(q)$ curve. For our model sequences ‘D’ and ‘E,’ we see that $q_{\text{crit}} \lesssim 2/3$, consistent with the mass-transfer stability limit that has already received much attention in the literature (Frank, Tohline & Even 2009).

4. Summary and Conclusions

Based on the earlier work of the Hachisu (1986a,b) and Hachisu, Eriguchi, & Nomoto (1986a) we have developed a self-consistent-field technique that can be used to construct equilibrium models of synchronously rotating DWD binaries having a range of total masses, mass ratios, and binary separations. In addition to effects introduced by synchronous rotation, the distorted structure of both stars in each converged model is governed by the zero-temperature white dwarf equation of state (1) and a self-consistently determined, Newtonian gravitational field. In an effort to illustrate the technique’s capabilities, we have constructed a set of models along five sequences: Three sequences (‘A’, ‘B’, and ‘C’) mimic the last segment of the detached “inspiral” phase of DWD binary evolutions during which both M_{tot} and q are held constant as a decreases; and two sequences (‘D’ and ‘E’) mimic a semi-detached “conservative mass transfer” phase of evolution during which M_{tot} is held fixed and the less massive star stays in marginal contact with its Roche lobe, but q steadily decreases while a steadily increases.

Along each inspiral sequence, the functional dependence of J_{tot} and E_{tot} on the orbital separation can be well understood in terms of simple analytical expressions that describe two spinning spherical white dwarfs in circular orbit about one another. For a given total mass and separation, the calculated orbital frequencies along each inspiral sequence deviate measurably from associated Keplerian frequencies only in models for which the Roche-lobe filling factor of the less-massive star is $\gtrsim 60\%$. But, at least for the sequences examined here, the deviation from Keplerian frequencies is never more than 1% even at contact.

Along both conservative mass-transfer sequences, we have documented how a , Ω , J_{tot} and E_{tot} vary with the system mass ratio as q decreases by roughly a factor of two, from $q = 1.0$ down to $q \lesssim 0.5$. Along each sequence we have compared our numerically determined values of a at various values of q with the analytic $a(q)$ function (47) that is derived by setting the radius of the less massive star, as specified by the Nauenberg (1972) mass-radius relation, equal to the Roche-lobe radius, as approximated by Eggleton (1983). Qualitatively, our results show the same $a(q)$ behavior that is predicted by this analytic expression. However, at a given q the value of a derived from our models is consistently $\sim 8\%$ larger than the value obtained from Eq. (47). The analytic expression could be brought into closer quantitative agreement with our numerical results if the leading coefficient in Eq. (47) is increased by 8%, that is, if the expression’s leading coefficient is changed from 0.0229 to 0.0247. This modification will, in turn, decrease the Keplerian frequency obtained from the analytic $a(q)$ expression by $\sim 9\%$, simultaneously bringing the analytically predicted orbital frequency into much closer agreement with our numerically determined values of Ω . Along both of our conservative mass-transfer sequences, the plot of $J_{\text{tot}}(q)$ displays an extremum at a value of $q \lesssim 2/3$. The location of this extremum is almost certainly identifying the value of q_{crit} that is relevant along both sequences.

The development of this SCF technique was originally motivated by our desire to build models that would serve as good, “quiet” initial conditions for hydrodynamical simulations that are de-

signed to probe the onset and nonlinear development of mass-transfer instabilities in close, unequal-mass DWD binaries. The new computational tool that we have described in this paper achieves this objective.

We acknowledge valuable interactions that we have had with B. Bourdin, J. Frank, D. Marcelllo, P. M. Motl, and S. Ou over the course of this project. We also thank an anonymous referee for pointing us to a key reference from Hachisu’s collection of work during the mid-1980’s. This work has been supported, in part, by grants AST-0708551 and DGE-0504507 from the U.S. National Science Foundation and, in part, by grant NNX07AG84G from NASA’s ATP program. This research also has been made possible by grants of high-performance computing time on the TeraGrid (MCA98N043), at LSU, and across LONI (Louisiana Optical Network Initiative).

A. White Dwarf Mass-Radius Relationship

A.1. The Chandrasekhar Mass

Chandrasekhar (1935) was the first to construct models of spherically symmetric stars using the equation of state defined by Eq. (1) and, in so doing, demonstrated that the maximum mass of an isolated, nonrotating white dwarf is $M_{\text{ch}} = 1.44(\mu_e/2)M_{\odot}$, where μ_e is the number of nucleons per electron and, hence, depends on the chemical composition of the WD. A concise derivation of M_{ch} (although, at the time, it was referred to as M_3) is presented in Chapter *XI* of Chandrasekhar (1967), where we also find that the expressions for the two key coefficients in Eqs. (1) and (2) are,

$$A \equiv \frac{\pi m_e^4 c^5}{3h^3}, \tag{A1}$$

$$B\mu_e^{-1} \equiv \frac{8\pi m_p}{3} \left(\frac{m_e c}{h} \right)^3. \tag{A2}$$

Numerical values for A and $B\mu_e^{-1}$ are given here in Table A1 along with values of the physical constants c , h , m_e , and m_p that we have used (column 2) and that Chandrasekhar (1967) used (column 3) to determine the values of A and $B\mu_e^{-1}$. The derived analytic expression for the limiting mass is,

$$\mu_e^2 M_{\text{ch}} = 4\pi m_3 \left(\frac{2A}{\pi G} \right)^{3/2} \frac{\mu_e^2}{B^2} = 1.14205 \times 10^{34} \text{ g}, \tag{A3}$$

where the coefficient,

$$m_3 \equiv \left(-\xi^2 \frac{d\theta_3}{d\xi} \right)_{\xi=\xi_1(\theta_3)} = 2.01824, \tag{A4}$$

represents a structural property of $n = 3$ polytropes ($\gamma = 4/3$ gases) whose numerical value can be found in Chapter *IV*, Table 4 or Chandrasekhar (1967). We note as well that Chandrasekhar

(1967) identified a characteristic radius, ℓ_1 , for WDs given by the expression,

$$\ell_1 \mu_e \equiv \left(\frac{2A}{\pi G} \right)^{1/2} \frac{\mu_e}{B} = 7.71395 \times 10^8 \text{ cm}. \quad (\text{A5})$$

A.2. The “Nauenberg” Mass-Radius Relationship

Nauenberg (1972) derived an analytic approximation for the mass-radius relationship exhibited by isolated, spherical WDs that obey the ZTWD equation of state given in Eq. (1). Specifically, he offered an expression of the form,

$$R = R_0 \left[\frac{(1 - n^{4/3})^{1/2}}{n^{1/3}} \right], \quad (\text{A6})$$

where,

$$n \equiv \frac{M}{(\mu m_\mu) N_0}, \quad (\text{A7})$$

$$N_0 \equiv \frac{(3\pi^2 \zeta)^{1/2}}{\nu^{3/2}} \left[\frac{hc}{2\pi G (\mu m_\mu)^2} \right]^{3/2} = \frac{\mu_e^2 m_p^2}{(\mu m_\mu)^3} \left[\frac{4\pi \zeta}{m_3^2 \nu^3} \right]^{1/2} M_{\text{ch}}, \quad (\text{A8})$$

$$R_0 \equiv (3\pi^2 \zeta)^{1/3} \left[\frac{h}{2\pi m_e c} \right] N_0^{1/3} = \frac{(\mu_e m_p)}{(\mu m_\mu)} \left[\frac{4\pi \zeta}{\nu} \right]^{1/2} \ell_1, \quad (\text{A9})$$

m_μ is the atomic mass unit (see Table A1), μ is the mean molecular weight of the gas, and ζ and ν are two adjustable parameters in Nauenberg’s analytic approximation, both of which are expected to be of order unity. By assuming that the average particle mass denoted by Chandrasekhar (1967) as $(\mu_e m_p)$ is identical to the average particle mass specified by Nauenberg (1972) as (μm_μ) and, following Nauenberg’s lead, by setting $\nu = 1$ and²,

$$\zeta = \frac{m_3^2}{4\pi} = 0.324142, \quad (\text{A10})$$

in Eq. (A8) we see that,

$$(\mu m_\mu) N_0 = M_{\text{ch}}. \quad (\text{A11})$$

Hence, the denominator in (A7) becomes the Chandrasekhar mass. Furthermore, expressions (A9) and (A6) become, respectively,

$$\mu_e R_0 = m_3 (\ell_1 \mu_e) = 1.55686 \times 10^9 \text{ cm}, \quad (\text{A12})$$

²Actually, Nauenberg (1972) sets $\zeta = 0.323$.

and,

$$R = R_0 \left\{ \frac{[1 - (M/M_{\text{ch}})^{4/3}]^{1/2}}{(M/M_{\text{ch}})^{1/3}} \right\}. \quad (\text{A13})$$

Finally, by adopting the values of M_\odot and R_\odot listed in Table A1, we obtain essentially³ the identical approximate, analytic mass-radius relationship for ZTWDs presented in Eqs. (27) and (28) of Nauenberg (1972):

$$\frac{R}{R_\odot} = \frac{0.0224}{\mu_e} \left\{ \frac{[1 - (M/M_{\text{ch}})^{4/3}]^{1/2}}{(M/M_{\text{ch}})^{1/3}} \right\}, \quad (\text{A14})$$

where,

$$\frac{M_{\text{ch}}}{M_\odot} = \frac{5.742}{\mu_e^2}. \quad (\text{A15})$$

A.3. The “Eggleton” Mass-Radius Relationship

Verbunt & Rappaport (1988) introduced the following approximate, analytic expression for the mass-radius relationship of a “completely degenerate ... star composed of pure helium” (*i.e.*, $\mu_e = 2$), attributing its origin to Eggleton (private communication):

$$\frac{R}{R_\odot} = 0.0114 \left[\left(\frac{M}{M_{\text{ch}}} \right)^{-2/3} - \left(\frac{M}{M_{\text{ch}}} \right)^{2/3} \right]^{1/2} \left[1 + 3.5 \left(\frac{M}{M_p} \right)^{-2/3} + \left(\frac{M}{M_p} \right)^{-1} \right]^{-2/3}, \quad (\text{A16})$$

where M_p is a constant whose numerical value is $0.00057M_\odot$. This “Eggleton” mass-radius relationship has been used widely by researchers when modeling the evolution of semi-detached binary star systems in which the donor is a ZTWD. Since the Nauenberg (1972) mass-radius relationship (A14) is retrieved from Eq. (A16) in the limit $M/M_p \gg 1$, it seems clear that Eggleton’s contribution was the insertion of the term in square brackets involving the ratio M/M_p which, as Marsh et al. (2004) phrase it, “allows for the change to a constant density configuration at low masses (Zapolsky & Salpeter 1969).” In this paper we have only constructed binary star systems in which the internal structure of both stars is governed by the ZTWD equation of state (1). Hence it is appropriate for us to compare the properties of our modeled systems to behaviors predicted by the “Nauenberg,” not the “Eggleton,” mass-radius relationship.

³The numerical coefficients that appear here in Eqs. (A14) and (A15) differ slightly from the ones presented in Eqs. (27) and (28), respectively, of Nauenberg (1972) presumably because the values of the physical constants — such as M_\odot and R_\odot — that we have adopted in this paper (see Table A1) are slightly different from the values adopted by Nauenberg.

REFERENCES

- Anderson, S. F., et al. 2005, *AJ*, 130, 2230
- Balay, S., Buschelman, K., Eijkhout, V., Gropp, W., Kaushik, D., Knepley, M., McInnes, L., Smith, B., and Zhang, H. 2004, *PETSc Users Manual*, ANL-95/11 - Revision 2.1.5
- Bender, P. L. 1998, *BAAS*, 30, 1326
- Benz, W., Cameron, A. G. W., Press, W. H., & Bowers, R.L. 1990, *ApJ*, 348,647
- Chandrasekhar, S. 1935, *MNRAS*, 95, 207
- Chandrasekhar, S. 1967, *An Introduction to the Study of Stellar Structure*, New York: Dover
- Clayton, G. C., Geballe, T. R., Herwig, F., Fryer, C., & Asplund, M. 2007, *ApJ*, 662, 1220
- Cohl, H. and Tohline, J. 1999, *ApJ*, 527, 86
- Cornish, N. J., & Larson, S. L. 2003, *Phys. Rev. D*, 67, 103001
- Cox, A. N. 2000, *Allen's Astrophysical Quantities*, 4th edition, New York: Springer-Verlag
- Dan, M., Rosswog, S., & Brüggen, M. 2008 (arXiv:0811.1517)
- D'Souza, M. C. R., Motl, P. M., Tohline, J. E., & Frank, J. 2006, *ApJ*, 643, 381
- Eggleton, P. P. 1983, *ApJ*, 268, 368
- Evans, C. R., Iben, I., Jr., & Smarr, L. 1987, *ApJ*, 323, 129
- Faller, J. E., & Bender, P. L. 1984, in *Precision Measurement and Fundamental Constants II*, ed., B. N. Taylor & W. D. Phillips (NBS Spec. Pub. 617; Washington, DC: NBS), 689
- Frank, J. 2008, *New Astronomy Reviews*, 51, 878
- Frank, J., Tohline, J. E. and Even, W. 2009, *ApJ*, in preparation
- Fryer, C. L., & Diehl, S. 2008, *ASP Conf. Series*, *Hydrogen Deficient Stars*, ed. K. Werner & T. Rauch, 391, 335
- Fryer, C. L., Woosley, S. E., Herant, M., & Davies, M. B. 1999, *ApJ*, 520, 650
- Gokhale, V., Peng, X. M., & Frank, J. 2007, *ApJ*, 655, 1010
- Guerrero, J., Garcia-Berro, E., & Isern, J. 2004, *A&A*, 413, 257
- Hachisu, I. 1986a, *ApJS*, 61, 479
- Hachisu, I. 1986b, *ApJS*, 62, 461

- Hachisu, I., Eriguchi, Y., & Nomoto, K. 1986a, ApJ, 308, 161
- Hachisu, I., Eriguchi, Y., & Nomoto, K. 1986b, ApJ, 311, 214
- Hils, D., Bender, P. L., & Webbink, R. F. 1990, ApJ, 360, 75
- Iben, I. J., & Tutukov, A. V. 1984, ApJS, 55, 335
- Iben, I. J., & Tutukov, A. V. 1986, ApJ, 311, 753
- Iben, I. J., Tutukov, A. V., & Yungelson, L. R. 1996, ApJ, 456, 750
- Karl, C. A., Napiwotzki, R., Nelemans, G., Christlieb, N., Koester, D., Heber, U., & Reimers, D. 2003, A&A, 410, 663
- Kopparapu, R. K., & Tohline, J. E. 2007, ApJ, 655, 1025
- Livio, M. 2000, in *Type Ia Supernovae: Theory and Cosmology*, ed. J. C. Niemeyer, & J. W. Truran (Cambridge Univ. Press), 33
- Marsh, T. R. 2000, NewAR, 44, 119
- Marsh, T. R., Nelemans, G., & Steeghs, D. 2004, MNRAS, 350, 113
- Maxted, P. F. L., Marsh, T. R., & Moran, C. K. 2000, MNRAS, 319, 305
- Motl, M. P., Frank, J., Tohline, J. E., & D’Souza, M. C. R. 2007, ApJ, 670, 1314
- Napiwotzki, R., Christlieb, N., Drechsel, H., Hagen, H.-J., Heber, U., Homeier, D., Karl, C., Koester, D., Leibundgut, B., Marsh, T. R., Moehler, S., Nelemans, G., Pauli, E.-M., Reimers, D., Renzini, A., & Yungelson, L. 2001, *Astronomische Nachrichten*, 322, 411
- Napiwotzki, R., Koester, D., Nelemans, G., Yungelson, L., Christlieb, N., Renzini, A., Reimers, D., Drechsel, H., & Leibundgut, B. 2002, A&A, 386, 957
- Napiwotzki, R., et al. 2004, in ASP Conf. Ser. 318, *Spectroscopically and Spatially Resolving the Components of Close Binary Stars*, ed. R. W. Hilditch, H. Hensberge, & K. Pavlovski (San Francisco: ASP), 402
- Nauenberg, M. 1972, ApJ, 175, 417
- Nelemans, G. 2005, in ASP Conf. Ser. 330, *The Astrophysics of Cataclysmic Variables and Related objects*, ed. J.-M. Hameury & J.-P. Lasota (San Francisco: ASP), 27
- Nelemans, G., Napiwotzki, R., Karl, C., Marsh, T. R., Voss, B., Roelofs, G., Izzard, R. G., Montgomery, M., Reerink, T., Christlieb, N., & Reimers, D. 2005, A&A, 440, 1087
- New, C. B. Kimberly, and Tohline, Joel E. 1997, ApJ, 490, 311

- Ostriker, J.P., and Mark, J W-K. 1964, ApJ, 151, 1075
- Paczynski, P. 1967, Acta Astron., 17, 287
- Ramsay, G., Brocksopp, C., Groot, P. J., Hakala, P., Lehto, H., Marsh, T. R., Napiwotzki, R., Nelemans, G., Potter, S., Slee, B., Steeghs, D., & Wu, K. 2007, ASP Conference Series, 15th *European Workshop on White Dwarfs*, 372, 425 (arXiv:astro-ph/0610357v1)
- Rasio, F. A., & Shapiro, S. L. 1995, ApJ, 438, 887
- Roelofs, G. H. A., Groot, P. J., Marsh, T. R., Steeghs, D., Barros, S. C. C., & Nelemans, G. 2005, MNRAS, 361, 487
- Ruciński, S. M. 1988, AJ, 95, 1895
- Segretain, L., Chabrier, G., & Mochkovitch, R. 1997, ApJ, 481, 355
- Verbunt, F., & Rappaport, S. 1988, ApJ, 332, 193
- Warner, B. 1995, Ap&SS, 225, 249
- Webbink, R. F., 1984, ApJ, 277, 355
- Woudt, P. A., & Warner, B. 2003, MNRAS, 345, 1266
- Yoon, S.-C., Podsiadlowski, Ph., & Rosswog, S. 2007, MNRAS, 380, 933
- Zapolsky, H. S., & Salpeter, E. E. 1969, ApJ, 158, 809

Table 1. Convergence of SCF Method: Binary Model B3

N_ϖ	N_θ	N_z	δ	VE
64	128	33	1.0×10^{-2}	4.5×10^{-3}
			1.0×10^{-3}	2.6×10^{-3}
			1.4×10^{-4}	2.2×10^{-3}
128	256	65	1.0×10^{-2}	4.0×10^{-3}
			1.0×10^{-3}	9.1×10^{-4}
			1.0×10^{-4}	5.7×10^{-4}
			3.5×10^{-5}	5.4×10^{-4}

Table 2. Sequence of single, nonrotating ZTWDs.

M (M_{\odot})	R (10^8 cm)	ρ_{\max} (g cm^{-3})	x_{\max}	I (10^{50} g cm 2)	k	VE
0.0844	19.7673	3.1623×10^4	0.2526	1.3317	0.2036	1.4×10^{-5}
0.1113	17.9368	5.6234×10^4	0.3060	1.4422	0.2031	6.1×10^{-5}
0.1460	16.2672	1.0000×10^5	0.3708	1.5508	0.2024	1.4×10^{-5}
0.1903	14.7421	1.7783×10^5	0.4492	1.6517	0.2015	5.8×10^{-5}
0.2457	13.3464	3.1623×10^5	0.5442	1.7360	0.2001	1.4×10^{-5}
0.3134	12.0666	5.6234×10^5	0.6593	1.7936	0.1983	5.8×10^{-5}
0.3938	10.8906	1.0000×10^6	0.7988	1.8133	0.1958	5.9×10^{-5}
0.4859	9.8078	1.7783×10^6	0.9678	1.7852	0.1926	1.6×10^{-5}
0.5873	8.8097	3.1623×10^6	1.1725	1.7051	0.1887	6.1×10^{-5}
0.6942	7.8896	5.6234×10^6	1.4205	1.5754	0.1839	5.8×10^{-5}
0.8018	7.0419	1.0000×10^7	1.7209	1.4058	0.1783	7.6×10^{-5}
0.9058	6.2628	1.7783×10^7	2.0850	1.2122	0.1721	6.6×10^{-5}
1.0022	5.5487	3.1623×10^7	2.5260	1.0111	0.1653	5.1×10^{-5}
1.0882	4.8961	5.6234×10^7	3.0603	0.8176	0.1581	6.3×10^{-5}
1.1624	4.3023	1.0000×10^8	3.7076	0.6429	0.1507	6.3×10^{-5}
1.2246	3.7643	1.7783×10^8	4.4919	0.4929	0.1433	7.0×10^{-5}
1.2753	3.2793	3.1623×10^8	5.4421	0.3698	0.1360	7.4×10^{-5}
1.3155	2.8443	5.6234×10^8	6.5932	0.2723	0.1290	9.0×10^{-5}
1.3469	2.4560	1.0000×10^9	7.9879	0.1972	0.1225	1.1×10^{-4}
1.3708	2.1116	1.7783×10^9	9.6775	0.1410	0.1164	1.2×10^{-4}
1.3887	1.8078	3.1623×10^9	11.7246	0.0997	0.1108	1.3×10^{-4}
1.4020	1.5414	5.6234×10^9	14.2047	0.0699	0.1058	1.4×10^{-4}
1.4116	1.3092	1.0000×10^{10}	17.2094	0.0486	0.1013	1.4×10^{-4}

Table 3. Selected single, nonrotating ZTWDs.

M (M_{\odot})	R (10^8 cm)	ρ_{\max} (g cm^{-3})	x_{\max}	k	W (10^{50} ergs)	U (10^{50} ergs)	Π (10^{50} ergs)
0.5019	9.6383	1.9536×10^6	0.9979	0.1923	-0.6130	0.3326	0.2044
0.6022	8.6713	3.4341×10^6	1.2043	0.1889	-0.9932	0.5526	0.3311
0.7522	7.4244	7.6648×10^6	1.5739	0.1813	-1.8512	1.0757	0.6171
0.9028	6.2847	1.7483×10^7	2.0718	0.1726	-3.2433	1.9860	1.0812
1.0025	5.5456	3.1703×10^7	2.5265	0.1655	-4.6465	2.9644	1.5490

Table 4. DWD Inspiral Sequence ‘A’: $M_{\text{tot}} = 1.5M_{\odot}$; $q = 1$

Model	a (10^9 cm)	Ω (10^{-2} s $^{-1}$)	M_{tot} (M_{\odot})	q	J_{tot} (10^{50} cgs)	E_{tot} (10^{50} erg)	VE
A1	2.0956	14.8480	1.5045	1.0000	5.3879	−1.8624	2.7×10^{-4}
A2	2.0970	14.8317	1.5043	1.0000	5.3881	−1.8618	2.8×10^{-4}
A3	2.1042	14.7493	1.5036	1.0000	5.3882	−1.8589	2.8×10^{-4}
A4	2.1099	14.6847	1.5030	1.0000	5.3886	−1.8567	2.9×10^{-4}
A5	2.1162	14.6156	1.5031	1.0000	5.3915	−1.8566	2.7×10^{-4}
A6	2.1239	14.5339	1.5031	1.0000	5.3954	−1.8560	2.7×10^{-4}
A7	2.1428	14.3360	1.5032	1.0000	5.4059	−1.8549	2.8×10^{-4}
A8	2.1544	14.2154	1.5030	1.0000	5.4112	−1.8532	2.9×10^{-4}
A9	2.1671	14.0863	1.5029	1.0000	5.4180	−1.8519	2.9×10^{-4}
A10	2.1809	13.9475	1.5028	1.0000	5.4254	−1.8508	2.6×10^{-4}
A11	2.1960	13.7990	1.5027	1.0000	5.4337	−1.8490	2.7×10^{-4}
A12	2.2292	13.4849	1.5030	1.0000	5.4554	−1.8471	2.6×10^{-4}
A13	2.2479	13.3121	1.5027	1.0000	5.4665	−1.8448	2.7×10^{-4}
A14	2.2669	13.1429	1.5032	1.0000	5.4814	−1.8447	2.7×10^{-4}
A15	2.2880	12.9570	1.5030	1.0000	5.4944	−1.8421	2.7×10^{-4}
A16	2.3103	12.7655	1.5027	1.0000	5.5082	−1.8392	2.8×10^{-4}
A17	2.3572	12.3804	1.5029	1.0000	5.5423	−1.8359	2.8×10^{-4}
A18	2.3828	12.1772	1.5027	1.0000	5.5597	−1.8329	2.8×10^{-4}
A19	2.4092	11.9748	1.5028	1.0000	5.5792	−1.8307	2.8×10^{-4}
A20	2.4362	11.7751	1.5032	1.0000	5.6013	−1.8298	2.8×10^{-4}
A21	2.4652	11.5645	1.5030	1.0000	5.6221	−1.8265	2.9×10^{-4}
A22	2.5261	11.1442	1.5030	1.0000	5.6684	−1.8215	2.8×10^{-4}
A23	2.5584	10.9314	1.5030	1.0000	5.6928	−1.8185	2.9×10^{-4}
A24	2.5920	10.7176	1.5028	1.0000	5.7185	−1.8151	3.1×10^{-4}
A25	2.6264	10.5057	1.5029	1.0000	5.7457	−1.8127	3.0×10^{-4}
A26	2.6624	10.2904	1.5028	1.0000	5.7729	−1.8093	3.0×10^{-4}
A27	2.6991	10.0786	1.5029	1.0000	5.8016	−1.8068	2.9×10^{-4}
A28	2.7376	9.8598	1.5028	1.0000	5.8286	−1.8039	1.5×10^{-4}
A29	2.8175	9.4479	1.5031	1.0000	5.8981	−1.7984	3.2×10^{-4}
A30	2.8597	9.2377	1.5031	1.0000	5.9315	−1.7951	3.2×10^{-4}
A31	2.8784	9.1459	1.5027	1.0000	5.9440	−1.7925	3.2×10^{-4}
A32	2.9478	8.8242	1.5032	1.0000	6.0024	−1.7892	3.3×10^{-4}

Table 4—Continued

Model	a (10^9 cm)	Ω (10^{-2} s $^{-1}$)	M_{tot} (M_{\odot})	q	J_{tot} (10^{50} cgs)	E_{tot} (10^{50} erg)	VE
A33	2.9940	8.6120	1.5031	1.0000	6.0336	−1.7860	1.9×10^{-4}
A34	3.0420	8.4102	1.5031	1.0000	6.0738	−1.7827	2.1×10^{-4}
A35	3.0911	8.2099	1.5032	1.0000	6.1135	−1.7797	2.2×10^{-4}

Table 5. Individual Stellar Components along DWD Inspiral Sequence ‘A’

Model	M_1 (M_\odot)	R_1 (10^9 cm)	$\rho_{\max}^{i=1}$ (10^9 cgs)	$f_{\text{RL}}^{i=1}$	$J_{\text{spin}}^{i=1}$ (10^{50} cgs)	M_2 (M_\odot)	R_2 (10^9 cm)	$\rho_{\max}^{i=2}$ (10^9 cgs)	$f_{\text{RL}}^{i=2}$	$J_{\text{spin}}^{i=2}$ (10^{50} cgs)
A1	0.7522	0.7841	6.745	1.0000	0.2562	0.7522	0.7841	6.745	1.0000	0.2562
A2	0.7522	0.7840	6.745	0.9969	0.2559	0.7522	0.7840	6.745	0.9969	0.2559
A3	0.7518	0.7835	6.745	0.9838	0.2540	0.7518	0.7835	6.745	0.9838	0.2540
A4	0.7515	0.7831	6.745	0.9736	0.2526	0.7515	0.7831	6.745	0.9736	0.2526
A5	0.7516	0.7825	6.758	0.9614	0.2509	0.7516	0.7825	6.758	0.9615	0.2509
A6	0.7516	0.7817	6.771	0.9471	0.2489	0.7516	0.7817	6.771	0.9471	0.2489
A7	0.7516	0.7798	6.805	0.9134	0.2441	0.7516	0.7798	6.805	0.9134	0.2441
A8	0.7515	0.7790	6.820	0.8942	0.2414	0.7515	0.7790	6.820	0.8942	0.2414
A9	0.7514	0.7780	6.837	0.8739	0.2384	0.7514	0.7780	6.837	0.8739	0.2384
A10	0.7514	0.7769	6.855	0.8523	0.2353	0.7514	0.7769	6.855	0.8523	0.2353
A11	0.7513	0.7759	6.876	0.8303	0.2320	0.7513	0.7758	6.876	0.8303	0.2320
A12	0.7515	0.7735	6.924	0.7838	0.2250	0.7515	0.7735	6.924	0.7838	0.2250
A13	0.7514	0.7724	6.944	0.7602	0.2213	0.7514	0.7724	6.944	0.7602	0.2213
A14	0.7516	0.7711	6.977	0.7367	0.2176	0.7516	0.7711	6.977	0.7367	0.2176
A15	0.7515	0.7701	6.992	0.7131	0.2138	0.7515	0.7701	6.992	0.7131	0.2138
A16	0.7513	0.7692	7.013	0.6903	0.2099	0.7513	0.7692	7.013	0.6903	0.2099
A17	0.7515	0.7668	7.062	0.6440	0.2020	0.7515	0.7668	7.062	0.6440	0.2020
A18	0.7514	0.7658	7.083	0.6215	0.1980	0.7514	0.7658	7.083	0.6215	0.1980
A19	0.7514	0.7650	7.103	0.5998	0.1940	0.7514	0.7650	7.103	0.5998	0.1940
A20	0.7516	0.7637	7.137	0.5779	0.1901	0.7516	0.7637	7.137	0.5779	0.1901
A21	0.7515	0.7629	7.153	0.5568	0.1861	0.7515	0.7629	7.153	0.5567	0.1861
A22	0.7515	0.7611	7.198	0.5160	0.1781	0.7515	0.7611	7.198	0.5160	0.1781
A23	0.7515	0.7603	7.214	0.4964	0.1742	0.7515	0.7603	7.214	0.4964	0.1742
A24	0.7514	0.7596	7.234	0.4774	0.1703	0.7514	0.7596	7.234	0.4774	0.1703

Table 5—Continued

Model	M_1 (M_\odot)	R_1 (10^9 cm)	$\rho_{\max}^{i=1}$ (10^9 cgs)	$f_{\text{RL}}^{i=1}$	$J_{\text{spin}}^{i=1}$ (10^{50} cgs)	M_2 (M_\odot)	R_2 (10^9 cm)	$\rho_{\max}^{i=2}$ (10^9 cgs)	$f_{\text{RL}}^{i=2}$	$J_{\text{spin}}^{i=2}$ (10^{50} cgs)
A25	0.7515	0.7585	7.251	0.4583	0.1664	0.7515	0.7585	7.251	0.4583	0.1664
A26	0.7514	0.7579	7.271	0.4404	0.1625	0.7514	0.7579	7.271	0.4404	0.1625
A27	0.7514	0.7571	7.290	0.4231	0.1587	0.7514	0.7571	7.290	0.4231	0.1587
A28	0.7514	0.7562	7.309	0.4057	0.1548	0.7514	0.7562	7.309	0.4057	0.1548
A29	0.7516	0.7548	7.349	0.3733	0.1476	0.7516	0.7548	7.349	0.3733	0.1476
A30	0.7515	0.7541	7.363	0.3575	0.1440	0.7515	0.7541	7.363	0.3576	0.1440
A31	0.7513	0.7540	7.363	0.3478	0.1424	0.7513	0.7541	7.363	0.3518	0.1424
A32	0.7516	0.7529	7.397	0.3282	0.1369	0.7516	0.7529	7.397	0.3282	0.1369
A33	0.7515	0.7522	7.412	0.3142	0.1333	0.7515	0.7522	7.412	0.3142	0.1333
A34	0.7516	0.7517	7.425	0.3005	0.1299	0.7516	0.7517	7.425	0.3005	0.1299
A35	0.7516	0.7511	7.438	0.2874	0.1265	0.7516	0.7510	7.440	0.2873	0.1265

Table 6. DWD Inspiral Sequence ‘B’: $M_{\text{tot}} = 1.5M_{\odot}$; $q = 2/3$

Model	a (10^9 cm)	Ω (10^{-2} s $^{-1}$)	M_{tot} (M_{\odot})	q	J_{tot} (10^{50} cgs)	E_{tot} (10^{50} erg)	VE
<i>B1</i>	2.6679	10.2944	1.5042	0.6671	5.5888	−1.9460	6.0×10^{-4}
<i>B2</i>	2.6743	10.2576	1.5043	0.6667	5.5931	−1.9460	6.1×10^{-4}
<i>B3</i>	2.6819	10.2106	1.5037	0.6667	5.5951	−1.9436	6.0×10^{-4}
<i>B4</i>	2.6923	10.1491	1.5033	0.6664	5.6001	−1.9419	6.1×10^{-4}
<i>B5</i>	2.7039	10.0831	1.5036	0.6663	5.6090	−1.9420	6.0×10^{-4}
<i>B6</i>	2.7177	10.0040	1.5034	0.6665	5.6174	−1.9401	6.1×10^{-4}
<i>B7</i>	2.7487	9.8330	1.5035	0.6665	5.6403	−1.9383	6.2×10^{-4}
<i>B8</i>	2.7687	9.7249	1.5035	0.6664	5.6542	−1.9372	6.2×10^{-4}
<i>B9</i>	2.7902	9.6104	1.5033	0.6665	5.6684	−1.9348	6.3×10^{-4}
<i>B10</i>	2.8138	9.4879	1.5033	0.6664	5.6851	−1.9333	6.3×10^{-4}
<i>B11</i>	2.8388	9.3609	1.5033	0.6663	5.7034	−1.9318	6.4×10^{-4}
<i>B12</i>	2.8654	9.2290	1.5032	0.6665	5.7224	−1.9295	6.4×10^{-4}
<i>B13</i>	2.9196	8.9712	1.5034	0.6665	5.7638	−1.9267	6.5×10^{-4}
<i>B14</i>	2.9514	8.8246	1.5033	0.6665	5.7864	−1.9241	6.8×10^{-4}
<i>B15</i>	2.9850	8.6746	1.5031	0.6665	5.8108	−1.9215	6.8×10^{-4}
<i>B16</i>	3.0199	8.5240	1.5034	0.6664	5.8380	−1.9201	6.9×10^{-4}
<i>B17</i>	3.0567	8.3680	1.5031	0.6665	5.8638	−1.9170	7.0×10^{-4}
<i>B18</i>	3.0949	8.2123	1.5032	0.6665	5.8928	−1.9147	7.0×10^{-4}
<i>B19</i>	3.1350	8.0548	1.5034	0.6663	5.9238	−1.9132	7.2×10^{-4}
<i>B20</i>	3.1766	7.8955	1.5031	0.6665	5.9543	−1.9097	7.4×10^{-4}
<i>B21</i>	3.2199	7.7355	1.5032	0.6666	5.9870	−1.9074	7.5×10^{-4}
<i>B22</i>	3.2653	7.5743	1.5034	0.6664	6.0218	−1.9056	7.8×10^{-4}
<i>B23</i>	3.3554	7.2699	1.5033	0.6667	6.0905	−1.9002	8.1×10^{-4}
<i>B24</i>	3.4062	7.1070	1.5034	0.6666	6.1285	−1.8978	8.1×10^{-4}
<i>B25</i>	3.4590	6.9440	1.5034	0.6665	6.1681	−1.8951	8.5×10^{-4}
<i>B26</i>	3.5133	6.7821	1.5032	0.6666	6.2078	−1.8917	8.6×10^{-4}
<i>B27</i>	3.5700	6.6211	1.5033	0.6665	6.2506	−1.8893	8.8×10^{-4}
<i>B28</i>	3.6285	6.4611	1.5034	0.6665	6.2948	−1.8867	9.2×10^{-4}
<i>B29</i>	3.6892	6.3010	1.5032	0.6666	6.3387	−1.8832	9.3×10^{-4}
<i>B30</i>	3.7520	6.1432	1.5033	0.6666	6.3860	−1.8809	9.6×10^{-4}
<i>B31</i>	3.8171	5.9860	1.5034	0.6665	6.4340	−1.8783	9.9×10^{-4}
<i>B32</i>	3.8846	5.8298	1.5032	0.6667	6.4828	−1.8747	1.0×10^{-3}

Table 6—Continued

Model	a (10^9 cm)	Ω (10^{-2} s $^{-1}$)	M_{tot} (M_{\odot})	q	J_{tot} (10^{50} cgs)	E_{tot} (10^{50} erg)	VE
<i>B33</i>	3.9544	5.6759	1.5034	0.6666	6.5344	−1.8724	1.0×10^{-3}
<i>B34</i>	4.0270	5.5225	1.5034	0.6665	6.5874	−1.8698	1.1×10^{-3}
<i>B35</i>	4.1030	5.3681	1.5027	0.6666	6.6380	−1.8645	1.1×10^{-3}
<i>B36</i>	4.1801	5.2199	1.5031	0.6666	6.6951	−1.8628	1.1×10^{-3}
<i>B37</i>	4.2601	5.0741	1.5034	0.6666	6.7548	−1.8611	1.2×10^{-3}
<i>B38</i>	4.2667	5.0582	1.5030	0.6668	6.7529	−1.8596	1.1×10^{-3}
<i>B39</i>	4.3502	4.9129	1.5031	0.6667	6.8124	−1.8570	1.2×10^{-3}
<i>B40</i>	4.4375	4.7683	1.5032	0.6664	6.8739	−1.8548	1.2×10^{-3}
<i>B41</i>	4.5270	4.6269	1.5030	0.6666	6.9357	−1.8513	1.3×10^{-3}
<i>B42</i>	4.6192	4.4889	1.5032	0.6668	7.0011	−1.8487	1.3×10^{-3}
<i>B43</i>	4.7160	4.3508	1.5034	0.6666	7.0680	−1.8467	1.4×10^{-3}
<i>B44</i>	4.8164	4.2143	1.5031	0.6667	7.1344	−1.8429	1.4×10^{-3}
<i>B45</i>	4.9203	4.0808	1.5029	0.6668	7.2039	−1.8395	1.5×10^{-3}
<i>B46</i>	5.0281	3.9494	1.5029	0.6668	7.2752	−1.8366	1.5×10^{-3}
<i>B47</i>	5.1405	3.8227	1.5033	0.6665	7.3562	−1.8352	1.7×10^{-3}
<i>B48</i>	5.1467	3.8136	1.5032	0.6669	7.3567	−1.8347	1.6×10^{-3}
<i>B49</i>	5.2630	3.6870	1.5033	0.6670	7.4330	−1.8320	1.7×10^{-3}

Table 7. Individual Stellar Components along DWD Inspiral Sequence ‘B’

Model	M_1 (M_\odot)	R_1 (10^9 cm)	$\rho_{\max}^{i=1}$ (10^9 cgs)	$f_{\text{RL}}^{i=1}$	$J_{\text{spin}}^{i=1}$ (10^{50} cgs)	M_2 (M_\odot)	R_2 (10^9 cm)	$\rho_{\max}^{i=2}$ (10^9 cgs)	$f_{\text{RL}}^{i=2}$	$J_{\text{spin}}^{i=2}$ (10^{50} cgs)
<i>B1</i>	0.9023	0.6345	17.049	0.1913	0.1289	0.6019	0.9117	3.076	1.0001	0.2004
<i>B2</i>	0.9026	0.6344	17.049	0.1898	0.1283	0.6017	0.9113	3.076	0.9908	0.1995
<i>B3</i>	0.9022	0.6345	17.049	0.1881	0.1278	0.6015	0.9108	3.076	0.9805	0.1982
<i>B4</i>	0.9022	0.6343	17.049	0.1856	0.1270	0.6012	0.9101	3.076	0.9667	0.1966
<i>B5</i>	0.9023	0.6343	17.047	0.1832	0.1261	0.6013	0.9090	3.083	0.9504	0.1948
<i>B6</i>	0.9021	0.6343	17.059	0.1803	0.1250	0.6013	0.9078	3.089	0.9314	0.1927
<i>B7</i>	0.9022	0.6340	17.082	0.1737	0.1228	0.6013	0.9056	3.108	0.8916	0.1882
<i>B8</i>	0.9022	0.6336	17.085	0.1694	0.1213	0.6012	0.9043	3.115	0.8677	0.1854
<i>B9</i>	0.9020	0.6336	17.100	0.1654	0.1198	0.6012	0.9029	3.123	0.8430	0.1825
<i>B10</i>	0.9021	0.6334	17.112	0.1610	0.1182	0.6011	0.9017	3.134	0.8181	0.1795
<i>B11</i>	0.9022	0.6334	17.121	0.1565	0.1165	0.6011	0.9003	3.144	0.7917	0.1764
<i>B12</i>	0.9020	0.6332	17.139	0.1520	0.1148	0.6012	0.8987	3.153	0.7650	0.1732
<i>B13</i>	0.9022	0.6329	17.162	0.1432	0.1114	0.6013	0.8963	3.175	0.7172	0.1670
<i>B14</i>	0.9021	0.6326	17.177	0.1383	0.1095	0.6012	0.8950	3.184	0.6907	0.1636
<i>B15</i>	0.9020	0.6324	17.195	0.1335	0.1076	0.6011	0.8935	3.194	0.6644	0.1602
<i>B16</i>	0.9022	0.6323	17.203	0.1288	0.1056	0.6012	0.8925	3.203	0.6403	0.1568
<i>B17</i>	0.9020	0.6323	17.222	0.1241	0.1036	0.6011	0.8914	3.213	0.6158	0.1534
<i>B18</i>	0.9020	0.6318	17.241	0.1192	0.1016	0.6012	0.8902	3.223	0.5916	0.1500
<i>B19</i>	0.9022	0.6316	17.246	0.1145	0.0995	0.6012	0.8887	3.233	0.5675	0.1465
<i>B20</i>	0.9019	0.6315	17.268	0.1099	0.0975	0.6012	0.8879	3.242	0.5448	0.1431
<i>B21</i>	0.9020	0.6311	17.287	0.1053	0.0955	0.6012	0.8866	3.251	0.5219	0.1397
<i>B22</i>	0.9022	0.6311	17.294	0.1009	0.0933	0.6012	0.8856	3.261	0.5003	0.1364
<i>B23</i>	0.9020	0.6307	17.340	0.0928	0.0895	0.6013	0.8837	3.280	0.4605	0.1301
<i>B24</i>	0.9021	0.6304	17.353	0.0885	0.0874	0.6013	0.8829	3.285	0.4408	0.1268

Table 7—Continued

Model	M_1 (M_\odot)	R_1 (10^9 cm)	$\rho_{\max}^{i=1}$ (10^9 cgs)	$f_{\text{RL}}^{i=1}$	$J_{\text{spin}}^{i=1}$ (10^{50} cgs)	M_2 (M_\odot)	R_2 (10^9 cm)	$\rho_{\max}^{i=2}$ (10^9 cgs)	$f_{\text{RL}}^{i=2}$	$J_{\text{spin}}^{i=2}$ (10^{50} cgs)
<i>B25</i>	0.9021	0.6302	17.362	0.0844	0.0853	0.6012	0.8823	3.294	0.4219	0.1235
<i>B26</i>	0.9019	0.6303	17.384	0.0806	0.0833	0.6013	0.8814	3.301	0.4029	0.1203
<i>B27</i>	0.9021	0.6301	17.398	0.0767	0.0812	0.6012	0.8804	3.309	0.3846	0.1171
<i>B28</i>	0.9021	0.6297	17.409	0.0729	0.0792	0.6013	0.8791	3.316	0.3661	0.1140
<i>B29</i>	0.9019	0.6298	17.432	0.0694	0.0772	0.6013	0.8790	3.323	0.3500	0.1109
<i>B30</i>	0.9021	0.6292	17.445	0.0657	0.0752	0.6013	0.8780	3.330	0.3334	0.1078
<i>B31</i>	0.9021	0.6293	17.457	0.0624	0.0732	0.6013	0.8772	3.336	0.3174	0.1048
<i>B32</i>	0.9019	0.6288	17.480	0.0591	0.0712	0.6013	0.8768	3.343	0.3024	0.1019
<i>B33</i>	0.9020	0.6289	17.495	0.0560	0.0693	0.6013	0.8762	3.349	0.2879	0.0990
<i>B34</i>	0.9021	0.6291	17.504	0.0531	0.0674	0.6013	0.8753	3.355	0.2734	0.0961
<i>B35</i>	0.9017	0.6287	17.504	0.0501	0.0655	0.6011	0.8749	3.355	0.2597	0.0932
<i>B36</i>	0.9019	0.6285	17.531	0.0473	0.0636	0.6012	0.8746	3.365	0.2469	0.0905
<i>B37</i>	0.9021	0.6283	17.542	0.0447	0.0617	0.6013	0.8739	3.371	0.2344	0.0878
<i>B38</i>	0.9017	0.6284	17.542	0.0445	0.0616	0.6013	0.8739	3.371	0.2334	0.0875
<i>B39</i>	0.9018	0.6280	17.572	0.0419	0.0598	0.6013	0.8732	3.378	0.2212	0.0848
<i>B40</i>	0.9021	0.6276	17.572	0.0394	0.0579	0.6011	0.8728	3.378	0.2096	0.0822
<i>B41</i>	0.9018	0.6273	17.601	0.0371	0.0562	0.6012	0.8723	3.387	0.1984	0.0796
<i>B42</i>	0.9018	0.6274	17.631	0.0350	0.0545	0.6014	0.8712	3.392	0.1875	0.0771
<i>B43</i>	0.9021	0.6267	17.645	0.0328	0.0527	0.6013	0.8710	3.398	0.1774	0.0746
<i>B44</i>	0.9019	0.6272	17.645	0.0309	0.0510	0.6012	0.8709	3.398	0.1677	0.0722
<i>B45</i>	0.9017	0.6272	17.682	0.0290	0.0494	0.6012	0.8704	3.407	0.1583	0.0698
<i>B46</i>	0.9017	0.6265	17.682	0.0271	0.0478	0.6012	0.8699	3.407	0.1491	0.0674
<i>B47</i>	0.9020	0.6266	17.697	0.0254	0.0462	0.6012	0.8696	3.416	0.1405	0.0652
<i>B48</i>	0.9018	0.6266	17.726	0.0254	0.0461	0.6014	0.8695	3.419	0.1400	0.0650

Table 7—Continued

Model	M_1 (M_\odot)	R_1 (10^9 cm)	$\rho_{\max}^{i=1}$ (10^9 cgs)	$f_{\text{RL}}^{i=1}$	$J_{\text{spin}}^{i=1}$ (10^{50} cgs)	M_2 (M_\odot)	R_2 (10^9 cm)	$\rho_{\max}^{i=2}$ (10^9 cgs)	$f_{\text{RL}}^{i=2}$	$J_{\text{spin}}^{i=2}$ (10^{50} cgs)
<i>B49</i>	0.9018	0.6260	17.758	0.0237	0.0445	0.6015	0.8691	3.421	0.1318	0.0628

Table 8. DWD Inspiral Sequence ‘C’: $M_{\text{tot}} = 1.5M_{\odot}$; $q = 1/2$

Model	a (10^9 cm)	Ω (10^{-2} s $^{-1}$)	M_{tot} (M_{\odot})	q	J_{tot} (10^{50} cgs)	E_{tot} (10^{50} erg)	VE
<i>C1</i>	3.1807	7.9054	1.5043	0.5001	5.5568	−2.1635	1.2×10^{-3}
<i>C2</i>	3.1814	7.9025	1.5044	0.5001	5.5574	−2.1638	1.2×10^{-3}
<i>C3</i>	3.1865	7.8822	1.5039	0.5002	5.5582	−2.1615	1.2×10^{-3}
<i>C4</i>	3.2070	7.8041	1.5033	0.4997	5.5671	−2.1594	1.2×10^{-3}
<i>C5</i>	3.2208	7.7539	1.5038	0.4997	5.5780	−2.1605	1.2×10^{-3}
<i>C6</i>	3.2376	7.6922	1.5036	0.4998	5.5883	−2.1584	1.2×10^{-3}
<i>C7</i>	3.2573	7.6213	1.5034	0.4999	5.6009	−2.1566	1.2×10^{-3}
<i>C8</i>	3.2800	7.5404	1.5035	0.4998	5.6150	−2.1561	1.2×10^{-3}
<i>C9</i>	3.3051	7.4547	1.5038	0.4996	5.6329	−2.1566	1.2×10^{-3}
<i>C10</i>	3.3321	7.3618	1.5033	0.4999	5.6489	−2.1529	1.2×10^{-3}
<i>C11</i>	3.3617	7.2631	1.5032	0.4999	5.6680	−2.1511	1.2×10^{-3}
<i>C12</i>	3.4235	7.0659	1.5036	0.4999	5.7108	−2.1497	1.3×10^{-3}
<i>C13</i>	3.4601	6.9530	1.5036	0.4998	5.7349	−2.1483	1.3×10^{-3}
<i>C14</i>	3.4985	6.8369	1.5032	0.4999	5.7590	−2.1448	1.3×10^{-3}
<i>C15</i>	3.5391	6.7190	1.5033	0.5000	5.7867	−2.1432	1.3×10^{-3}
<i>C16</i>	3.5823	6.5967	1.5035	0.4998	5.8157	−2.1426	1.4×10^{-3}
<i>C17</i>	3.6274	6.4733	1.5035	0.4998	5.8463	−2.1405	1.4×10^{-3}
<i>C18</i>	3.6747	6.3467	1.5032	0.5000	5.8765	−2.1370	1.4×10^{-3}
<i>C19</i>	3.7245	6.2193	1.5032	0.4999	5.9102	−2.1353	1.4×10^{-3}
<i>C20</i>	3.7764	6.0914	1.5036	0.4998	5.9468	−2.1349	1.5×10^{-3}
<i>C21</i>	3.8311	5.9605	1.5034	0.4998	5.9826	−2.1320	1.5×10^{-3}
<i>C22</i>	3.8878	5.8291	1.5032	0.5001	6.0197	−2.1286	1.5×10^{-3}
<i>C23</i>	3.9475	5.6967	1.5032	0.4999	6.0592	−2.1266	1.6×10^{-3}
<i>C24</i>	4.0093	5.5658	1.5036	0.4998	6.1025	−2.1261	1.6×10^{-3}
<i>C25</i>	4.0742	5.4324	1.5034	0.4999	6.1443	−2.1232	1.7×10^{-3}
<i>C26</i>	4.1412	5.2995	1.5031	0.5001	6.1874	−2.1194	1.7×10^{-3}
<i>C27</i>	4.2115	5.1674	1.5031	0.5000	6.2340	−2.1173	1.8×10^{-3}
<i>C28</i>	4.2844	5.0359	1.5035	0.4999	6.2833	−2.1166	1.8×10^{-3}
<i>C29</i>	4.3605	4.9039	1.5035	0.4999	6.3327	−2.1146	1.9×10^{-3}
<i>C30</i>	4.4396	4.7723	1.5031	0.5001	6.3821	−2.1100	1.9×10^{-3}
<i>C31</i>	4.5218	4.6425	1.5031	0.5001	6.4355	−2.1076	2.0×10^{-3}
<i>C32</i>	4.6077	4.5130	1.5033	0.5000	6.4912	−2.1066	2.0×10^{-3}

Table 8—Continued

Model	a (10^9 cm)	Ω (10^{-2} s $^{-1}$)	M_{tot} (M_{\odot})	q	J_{tot} (10^{50} cgs)	E_{tot} (10^{50} erg)	VE
<i>C33</i>	4.6142	4.5018	1.5040	0.4996	6.4939	−2.1098	2.0×10^{-3}
<i>C34</i>	4.7030	4.3735	1.5033	0.5001	6.5480	−2.1038	2.1×10^{-3}
<i>C35</i>	4.7960	4.2462	1.5030	0.5001	6.6056	−2.1003	2.2×10^{-3}
<i>C36</i>	4.8938	4.1186	1.5027	0.5000	6.6642	−2.0972	2.2×10^{-3}

Table 9. Individual Stellar Components along DWD Inspiral Sequence ‘C’

Model	M_1 (M_\odot)	R_1 (10^9 cm)	$\rho_{\max}^{i=1}$ (10^9 cgs)	$f_{\text{RL}}^{i=1}$	$J_{\text{spin}}^{i=1}$ (10^{50} cgs)	M_2 (M_\odot)	R_2 (10^9 cm)	$\rho_{\max}^{i=2}$ (10^9 cgs)	$f_{\text{RL}}^{i=2}$	$J_{\text{spin}}^{i=2}$ (10^{50} cgs)
<i>C1</i>	1.0028	0.5542	31.824	0.0627	0.0800	0.5015	1.0110	1.767	1.0000	0.1613
<i>C2</i>	1.0029	0.5541	31.824	0.0626	0.0799	0.5015	1.0108	1.767	0.9987	0.1613
<i>C3</i>	1.0025	0.5544	31.824	0.0624	0.0798	0.5014	1.0104	1.767	0.9927	0.1607
<i>C4</i>	1.0025	0.5546	31.824	0.0612	0.0790	0.5009	1.0093	1.767	0.9703	0.1586
<i>C5</i>	1.0027	0.5541	31.806	0.0602	0.0784	0.5010	1.0081	1.772	0.9536	0.1571
<i>C6</i>	1.0025	0.5543	31.812	0.0593	0.0778	0.5011	1.0068	1.776	0.9334	0.1553
<i>C7</i>	1.0023	0.5547	31.834	0.0583	0.0771	0.5011	1.0051	1.780	0.9109	0.1534
<i>C8</i>	1.0024	0.5541	31.845	0.0568	0.0762	0.5010	1.0035	1.786	0.8873	0.1512
<i>C9</i>	1.0028	0.5540	31.823	0.0554	0.0753	0.5010	1.0021	1.791	0.8634	0.1489
<i>C10</i>	1.0023	0.5544	31.847	0.0542	0.0744	0.5010	1.0007	1.796	0.8375	0.1464
<i>C11</i>	1.0022	0.5541	31.878	0.0527	0.0734	0.5010	0.9993	1.801	0.8112	0.1438
<i>C12</i>	1.0024	0.5537	31.901	0.0497	0.0713	0.5011	0.9961	1.814	0.7593	0.1388
<i>C13</i>	1.0025	0.5537	31.901	0.0480	0.0701	0.5010	0.9943	1.819	0.7309	0.1360
<i>C14</i>	1.0022	0.5539	31.934	0.0465	0.0689	0.5010	0.9933	1.824	0.7048	0.1332
<i>C15</i>	1.0022	0.5537	31.965	0.0448	0.0677	0.5011	0.9919	1.829	0.6777	0.1303
<i>C16</i>	1.0025	0.5533	31.971	0.0431	0.0664	0.5010	0.9905	1.836	0.6507	0.1274
<i>C17</i>	1.0024	0.5533	31.982	0.0415	0.0651	0.5010	0.9887	1.841	0.6239	0.1245
<i>C18</i>	1.0021	0.5534	32.020	0.0399	0.0639	0.5010	0.9873	1.847	0.5983	0.1216
<i>C19</i>	1.0022	0.5532	32.053	0.0383	0.0625	0.5010	0.9861	1.852	0.5728	0.1187
<i>C20</i>	1.0025	0.5530	32.057	0.0366	0.0612	0.5011	0.9850	1.857	0.5488	0.1158
<i>C21</i>	1.0024	0.5530	32.072	0.0351	0.0598	0.5010	0.9834	1.863	0.5242	0.1129
<i>C22</i>	1.0021	0.5525	32.115	0.0335	0.0585	0.5011	0.9827	1.867	0.5012	0.1100
<i>C23</i>	1.0021	0.5530	32.152	0.0320	0.0572	0.5010	0.9815	1.873	0.4788	0.1072
<i>C24</i>	1.0025	0.5528	32.158	0.0305	0.0558	0.5011	0.9804	1.877	0.4571	0.1044

Table 9—Continued

Model	M_1 (M_\odot)	R_1 (10^9 cm)	$\rho_{\max}^{i=1}$ (10^9 cgs)	$f_{\text{RL}}^{i=1}$	$J_{\text{spin}}^{i=1}$ (10^{50} cgs)	M_2 (M_\odot)	R_2 (10^9 cm)	$\rho_{\max}^{i=2}$ (10^9 cgs)	$f_{\text{RL}}^{i=2}$	$J_{\text{spin}}^{i=2}$ (10^{50} cgs)
<i>C25</i>	1.0024	0.5522	32.175	0.0290	0.0544	0.5010	0.9793	1.882	0.4357	0.1015
<i>C26</i>	1.0020	0.5524	32.223	0.0276	0.0531	0.5011	0.9786	1.886	0.4154	0.0988
<i>C27</i>	1.0021	0.5523	32.267	0.0262	0.0517	0.5011	0.9775	1.891	0.3951	0.0960
<i>C28</i>	1.0024	0.5515	32.281	0.0248	0.0503	0.5011	0.9761	1.895	0.3755	0.0933
<i>C29</i>	1.0024	0.5515	32.291	0.0235	0.0489	0.5011	0.9753	1.899	0.3572	0.0906
<i>C30</i>	1.0020	0.5518	32.342	0.0223	0.0476	0.5011	0.9746	1.903	0.3393	0.0879
<i>C31</i>	1.0020	0.5516	32.397	0.0211	0.0463	0.5011	0.9739	1.907	0.3219	0.0853
<i>C32</i>	1.0022	0.5510	32.425	0.0199	0.0450	0.5011	0.9727	1.911	0.3049	0.0827
<i>C33</i>	1.0029	0.5505	32.425	0.0197	0.0448	0.5011	0.9727	1.911	0.3041	0.0825
<i>C34</i>	1.0021	0.5511	32.462	0.0187	0.0435	0.5011	0.9722	1.915	0.2883	0.0800
<i>C35</i>	1.0019	0.5508	32.522	0.0176	0.0422	0.5011	0.9720	1.919	0.2735	0.0775
<i>C36</i>	1.0018	0.5508	32.522	0.0166	0.0409	0.5009	0.9711	1.919	0.2582	0.0750

Table 10. Semi-detached DWD Sequence ‘D’; $M_{\text{tot}} = 1.5M_{\odot}$

M_{tot} (M_{\odot})	q	a (10^9 cm)	Ω (10^{-2} s $^{-1}$)	J_{tot} (10^{50} cgs)	E_{tot} (10^{50} erg)	VE
1.5048	1.0000	2.1010	14.8472	5.3866	−1.8636	1.5×10^{-4}
1.5034	0.9508	2.1638	14.1787	5.4116	−1.8566	1.8×10^{-4}
1.5045	0.8994	2.2336	13.4444	5.4491	−1.8611	9.5×10^{-5}
1.5034	0.8507	2.3102	12.8287	5.4797	−1.8628	1.4×10^{-4}
1.5033	0.8007	2.3961	12.1414	5.5141	−1.8736	2.2×10^{-4}
1.5034	0.7504	2.4919	11.4431	5.5460	−1.8925	3.1×10^{-4}
1.5034	0.7004	2.5987	10.7442	5.5702	−1.9194	4.0×10^{-4}
1.5034	0.6504	2.7188	10.0382	5.5871	−1.9572	5.5×10^{-4}
1.5032	0.6004	2.8550	9.3217	5.5914	−2.0072	7.2×10^{-4}
1.5033	0.5503	3.0109	9.0670	5.5804	−2.0741	9.1×10^{-4}
1.5031	0.5004	3.1914	7.8907	5.5484	−2.1587	1.2×10^{-3}

Table 11. Semi-detached DWD Sequence ‘E’; $M_{\text{tot}} = 1.0M_{\odot}$

M_{tot} (M_{\odot})	q	a (10^9 cm)	Ω (10^{-2} s $^{-1}$)	J_{tot} (10^{50} cgs)	E_{tot} (10^{50} erg)	VE
1.0030	1.0000	2.7109	8.2477	3.3579	−0.6657	1.7×10^{-4}
1.0024	0.9504	2.7778	7.9369	3.3687	−0.6642	1.6×10^{-4}
1.0019	0.9001	2.8641	7.5710	3.3850	−0.6636	2.1×10^{-4}
1.0022	0.8508	2.9380	7.2829	3.3983	−0.6659	2.2×10^{-4}
1.0024	0.8003	3.0161	6.9993	3.4073	−0.6698	2.2×10^{-4}
1.0024	0.7503	3.1165	6.6609	3.4163	−0.6751	2.6×10^{-4}
1.0024	0.7003	3.2294	6.3129	3.4212	−0.6828	3.3×10^{-4}
1.0023	0.6502	3.3569	5.9551	3.4204	−0.6934	3.9×10^{-4}
1.0023	0.6003	3.5026	5.5862	3.4123	−0.7074	4.7×10^{-4}
1.0022	0.5503	3.6696	5.2078	3.3943	−0.7254	5.6×10^{-4}
1.0021	0.5003	3.8649	4.8169	3.3644	−0.7484	6.8×10^{-4}
1.0020	0.4504	4.0955	4.4134	3.3184	−0.7773	8.0×10^{-4}

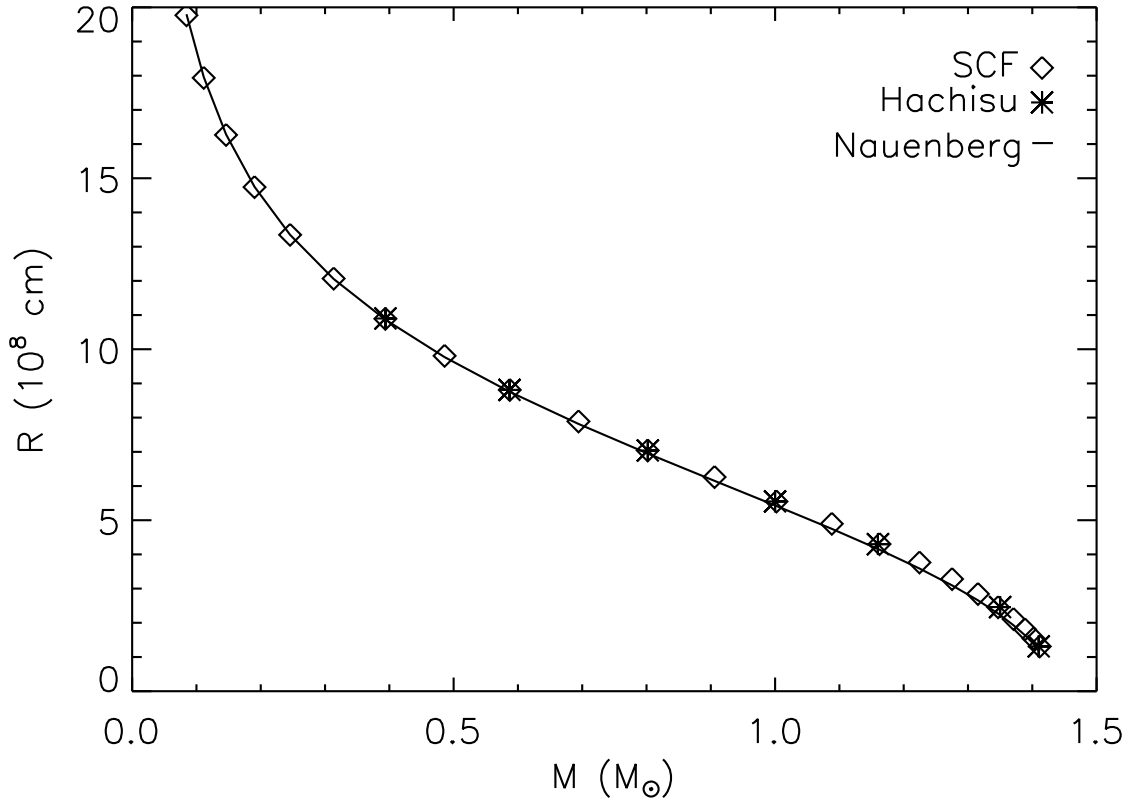


Fig. 1.— The mass-radius relationship is shown for spherical stars with our adopted ZTWD equation of state. Diamonds represent results derived using our three-dimensional SCF scheme applied to nonrotating, isolated configurations (see Table 2); asterisks show previously published results for the same equation of state taken from Hachisu (1986a); the solid curve shows the analytic mass-radius relation, Eq. (A14), derived by Nauenberg (1972).

Table A1. Physical Constants

Constants ^a (1)	This Paper ^b (2)	Chandrasekhar (1967) ^c (3)
c (cm s ⁻¹)	2.99792×10^{10}	2.9978×10^{10}
h (erg · s)	6.62608×10^{-27}	6.62×10^{-27}
m_e (g)	9.10939×10^{-28}	9.105×10^{-28}
m_p (g)	1.67262×10^{-24}	1.672×10^{-24}
m_μ (g)	1.66054×10^{-24}	...
G (cm ³ g ⁻¹ s ⁻²)	6.6726×10^{-8}	6.62×10^{-8}
M_\odot (g)	1.9891×10^{33}	1.985×10^{33}
R_\odot (cm)	6.955×10^{10}	6.951×10^{10}
A (dynes cm ⁻²)	6.00228×10^{22}	6.01×10^{22}
$B\mu_e^{-1}$ (g cm ⁻³)	9.81011×10^5	9.82×10^5
$\ell_1\mu_e$ (cm)	7.71395×10^8	7.705×10^8

^aSpeed of light, c ; Planck’s constant, h ; mass of the electron, m_e ; mass of the proton m_p ; atomic mass unit, m_μ ; universal gravitational constant, G ; solar mass, M_\odot ; solar radius, R_\odot ; as used in the ZTWD equation of state (1), $A = \pi m_e^4 c^5 / 3h^3$ and $B\mu_e^{-1} = 8\pi m_e^3 c^3 m_p / 3h^3$; the characteristic WD length scale, $\ell_1\mu_e = (2A/\pi G)^{1/2}(\mu_e/B)$.

^bDrawn from Cox (2000).

^cDrawn from Appendix I, Table 32 of Chandrasekhar (1967).

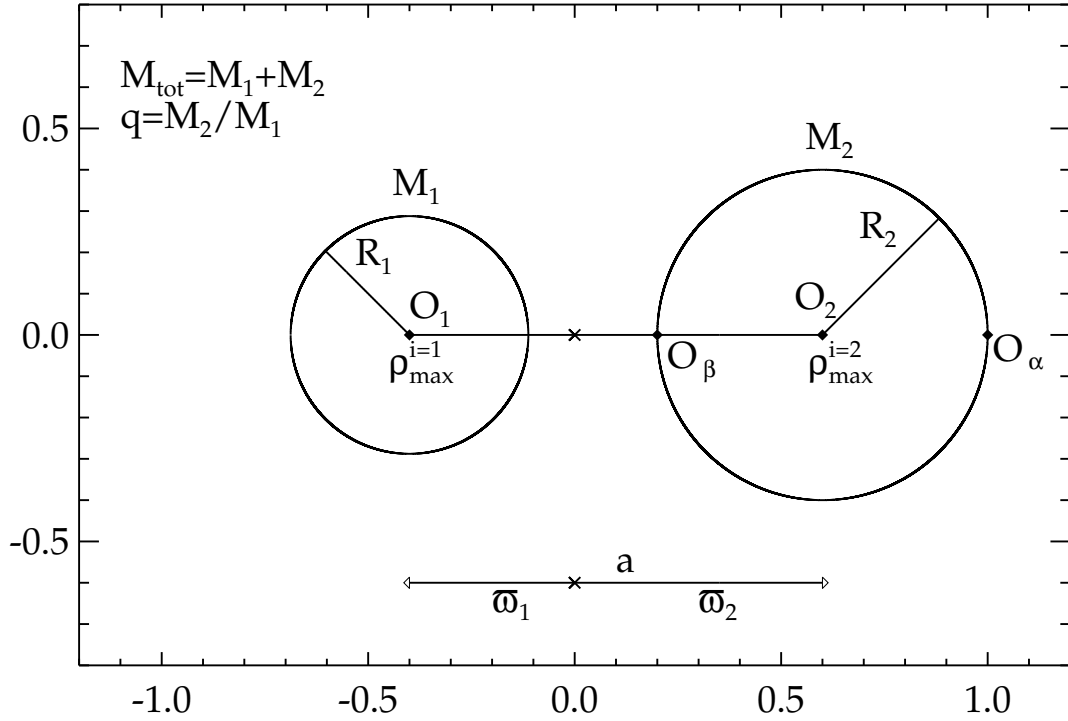


Fig. 2.— Schematic diagram illustrating the equatorial-plane structure of a binary star system. The primary star, on the left, has a mass M_1 , a radius R_1 , and a central density $\rho_{\max}^{i=1}$; the secondary star, on the right, has a mass $M_2 \leq M_1$, a radius R_2 , and a central density $\rho_{\max}^{i=2}$. The centers of mass of the two stars (points labeled O_1 and O_2) are separated by a distance $a = \varpi_1 + \varpi_2$, and their distances from the center of mass of the system are, respectively, ϖ_1 and ϖ_2 . The points labeled O_α and O_β identify, respectively, the outer edge and inner edge of the secondary star.

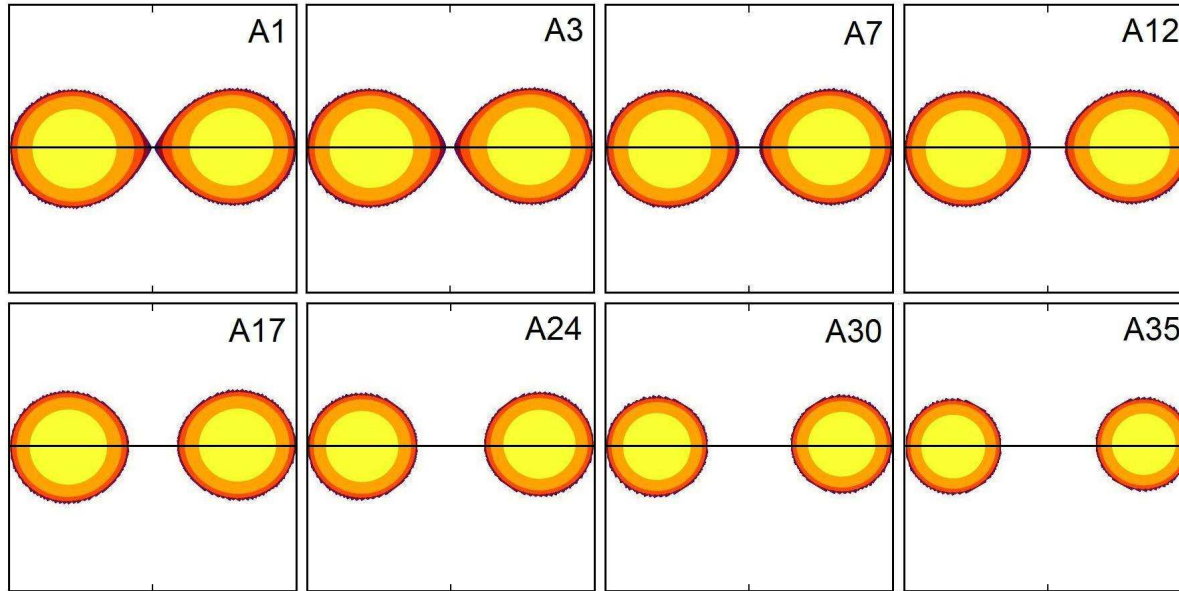


Fig. 3.— Density contours in the equatorial plane are shown for eight separate ZTWD binary models with increasing separation along inspiral sequence ‘A’ ($M_{\text{tot}} = 1.5M_{\odot}$; $q = 1$). Labels in the upper-right-hand corner of each panel identify each model by number according to its corresponding position along the sequence as itemized in Tables 4 and 5.

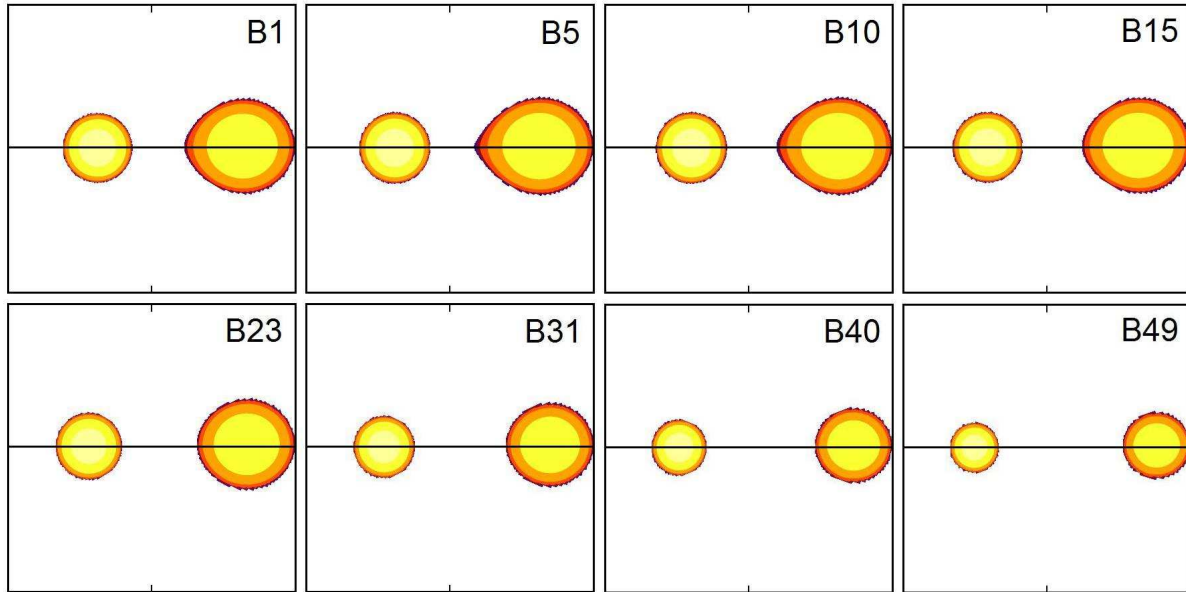


Fig. 4.— Density contours in the equatorial plane are shown for eight separate ZTWD binary models with increasing separation along inspiral sequence ‘B’ ($M_{\text{tot}} = 1.5M_{\odot}$; $q = 2/3$). Labels in the upper-right-hand corner of each panel identify each model by number according to its corresponding position along the sequence as itemized in Tables 6 and 7.

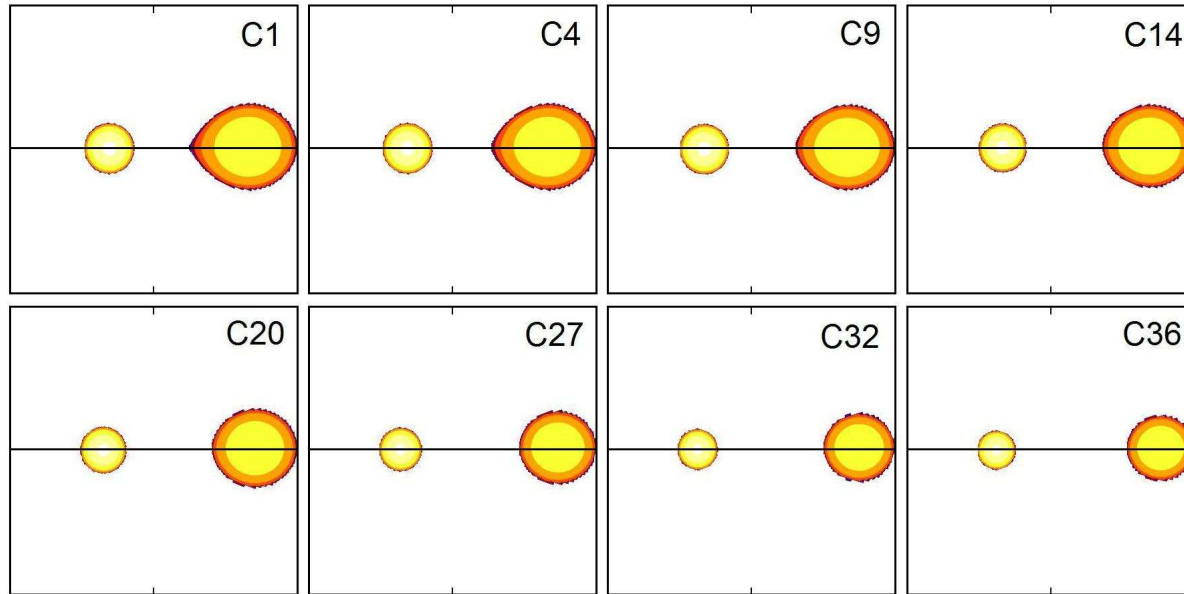


Fig. 5.— Density contours in the equatorial plane are shown for eight separate ZTWD binary models with increasing separation along inspiral sequence ‘C’ ($M_{\text{tot}} = 1.5M_{\odot}$; $q = 1/2$). Labels in the upper-right-hand corner of each panel identify each model by number according to its corresponding position along the sequence as itemized in Tables 8 and 9.

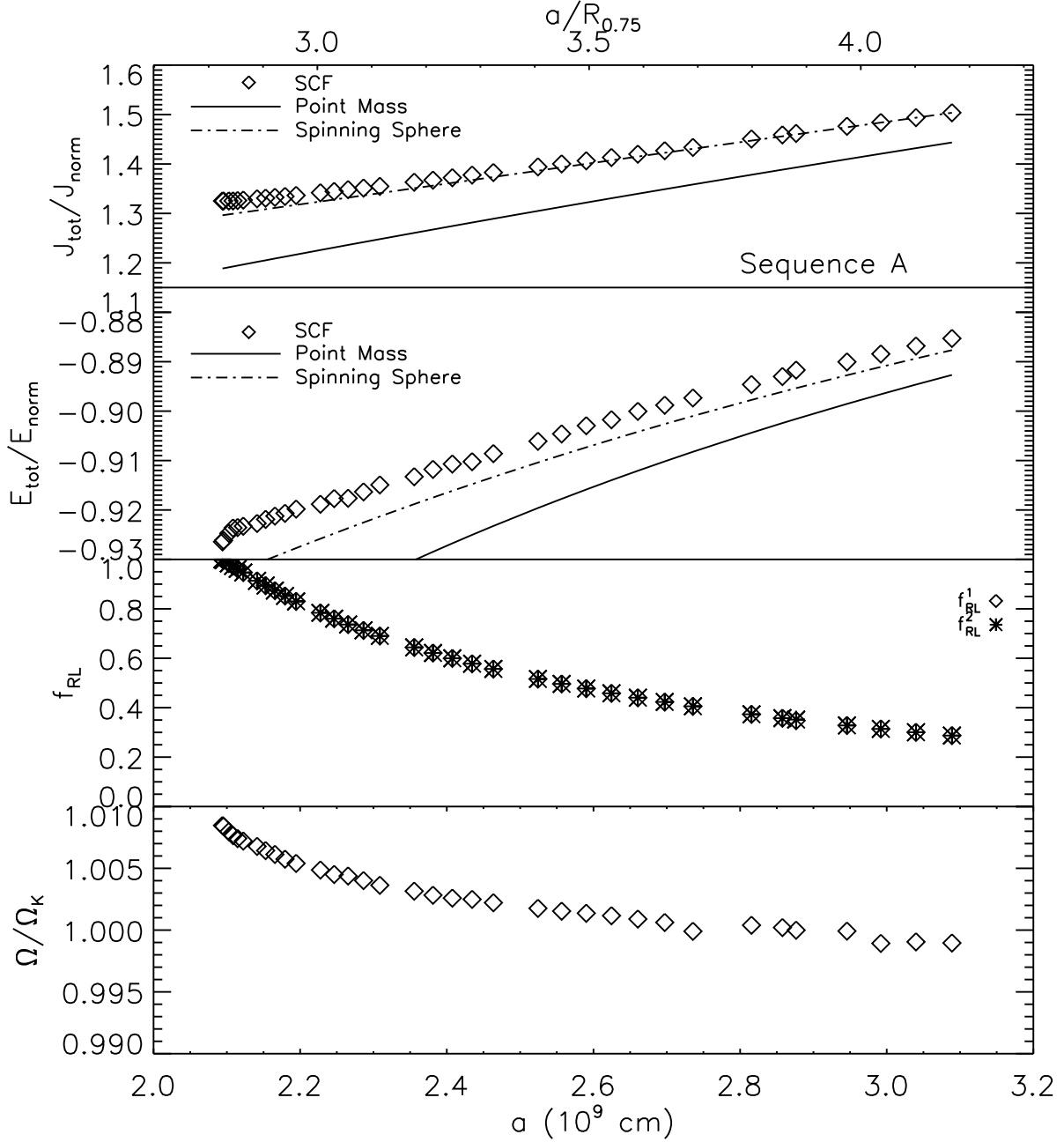


Fig. 6.— (*Top panel*) Normalized total angular momentum, $J_{\text{tot}}/J_{\text{norm}}$, (*second panel*) normalized total energy, $E_{\text{tot}}/E_{\text{norm}}$, (*third panel*) the Roche-lobe filling factor, f_{RL} , for the secondary (asterisks) and primary (diamonds) stars, and (*bottom panel*) the normalized orbital angular velocity, Ω/Ω_{K} , are plotted as a function of binary separation for models A1 through A35 along inspiral sequence ‘A’ ($M_{\text{tot}} = 1.5M_{\odot}$; $q = 1$). Data for the individual models is drawn from Tables 4 and 5; the separation a is labeled in units of 10^9 cm along the bottom axis and as a ratio to $R_{0.75}$ along the top axis. The solid curves in the top two panels display the analytic functions $J_{\text{pm}}(a)/J_{\text{norm}}$ and $E_{\text{pm}}(a)/E_{\text{norm}}$ given, respectively, by Eqs. (40) and (44) for a “point-mass” sequence of the specified total mass and mass ratio; and the dot-dashed curves display the analytic functions $J_{\text{ss}}(a)/J_{\text{norm}}$ and $E_{\text{ss}}(a)/E_{\text{norm}}$ appropriate for a “spinning spheres” sequence given, respectively, by Eqs. (41)

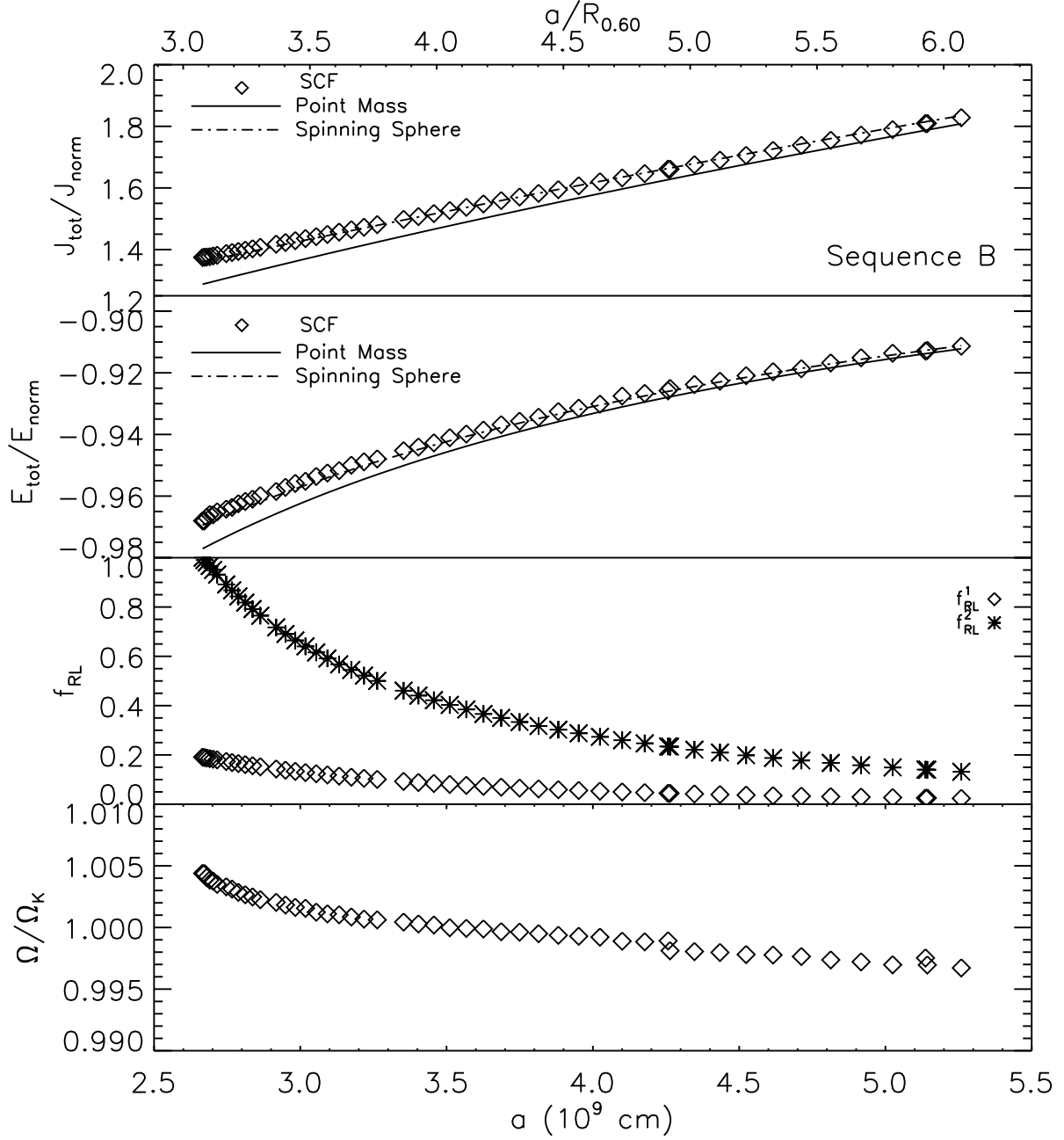


Fig. 7.— Same as Fig. 6 but for models $B1$ through $B49$ along the inspiral sequence ‘B’ ($M_{\text{tot}} = 1.5M_{\odot}$; $q = 2/3$), as tabulated in Tables 6 and 7; along the top axis, the separation a is labeled as a ratio to $R_{0.60}$.

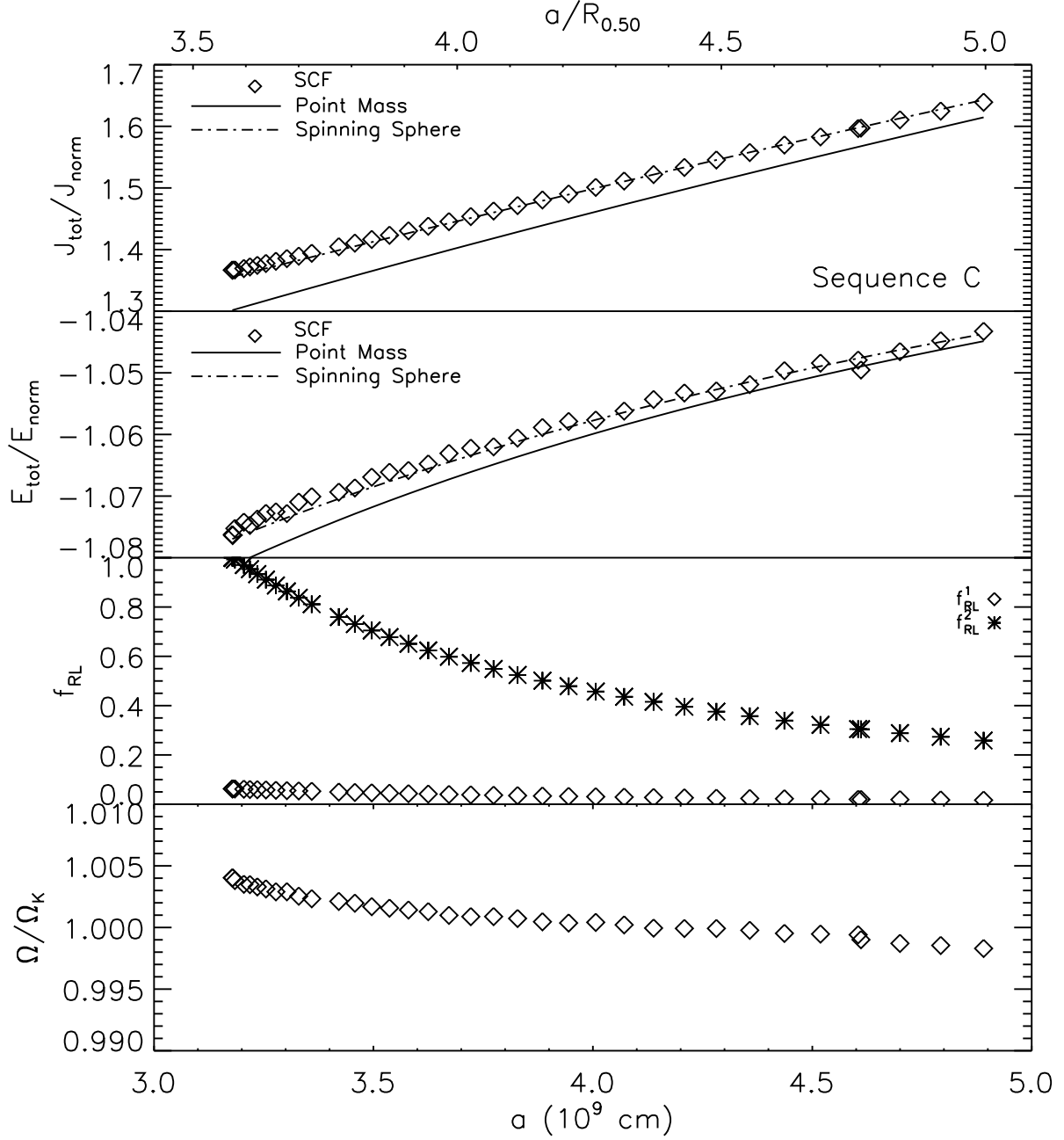


Fig. 8.— Same as Fig. 6 but for models $C1$ through $C36$ along the inspiral sequence ‘C’ ($M_{\text{tot}} = 1.5M_{\odot}$; $q = 1/2$), as tabulated in Tables 8 and 9; along the top axis, the separation a is labeled as a ratio to $R_{0.50}$.

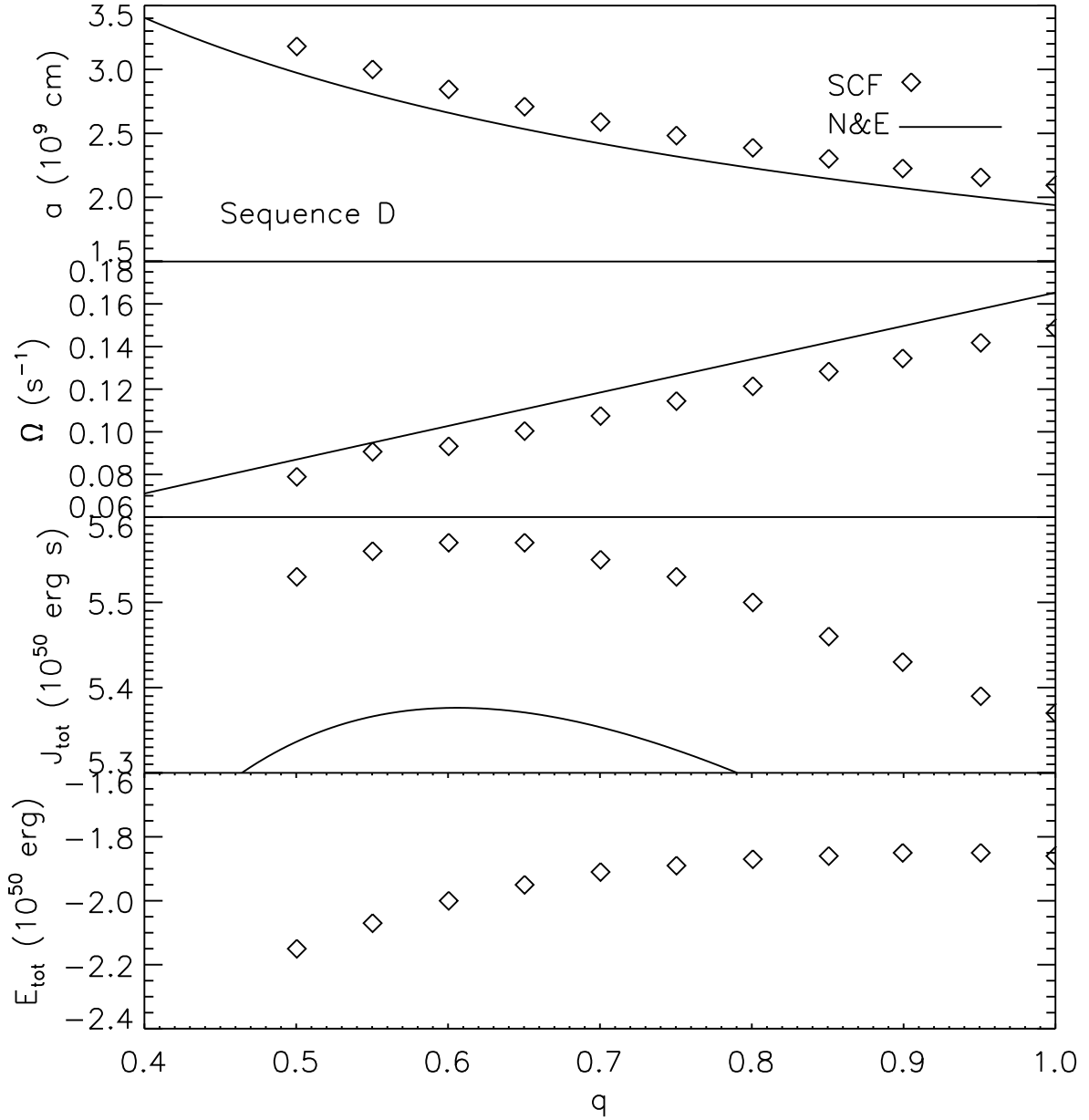


Fig. 9.— System parameters a , Ω , J_{tot} , and E_{tot} at contact as a function of mass ratio, q , for DWD systems having a total mass of $1.5M_{\odot}$. Solid curves in the top three panels show predicted behavior based on Nauenberg’s (1972) and Eggleton’s (1983) approximate, analytic expressions as discussed in the text.

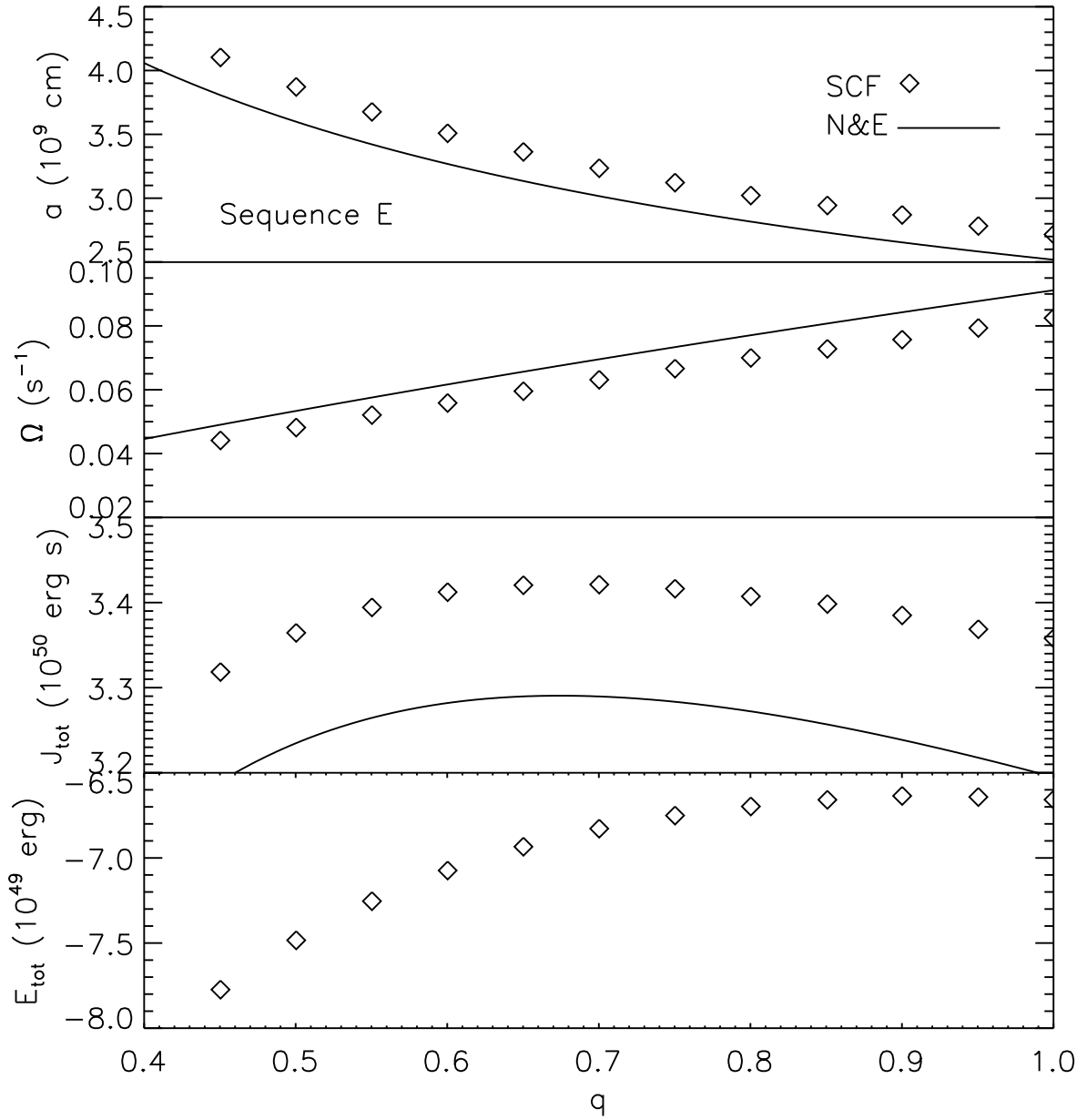


Fig. 10.— Same as Figure 9, but for DWD systems having a total mass of $1.0M_{\odot}$.